GULF GENERAL ATOMIC

Gulf-GA-A12635

GAS-COOLED FAST BREEDER REACTOR

QUARTERLY PROGRESS REPORT

FOR THE PERIOD FEBRUARY 1, 1973 THROUGH APRIL 30, 1973

by

Project Staff

Prepared for the
U.S. Atomic Energy Commission
San Francisco Operations Office
Under
Contract AT(04-3)-167
Project Agreement No. 23

Gulf General Atomic Project 393

June 15, 1973

GULF GENERAL ATOMIC COMPANY
P.O. BOX 81608, SAN DIEGO, CALIFORNIA 92138

PROGRESS REPORT SERIES

GA-5537	November 1, 1963 to July 31, 1964
GA-6667	August 1, 1964 to July 31, 1965
GA-7645	August 1, 1965 to July 31, 1966
GA-8107	August 1, 1966 to July 31, 1967
GA-8787	August 1, 1967 to July 31, 1968
GA-8895	August 1, 1968 through October 31, 1968
GA-9229	November 1, 1968 through January 31, 1969
GA-9359	February 1, 1969 through April 30, 1969
GA-9639	May 1, 1969 through July 31, 1969
GA-9811	August 1, 1969 through October 31, 1969
GA-9838	November 1, 1969 through January 31, 1970
GA-10517	February 1, 1970 through January 31, 1971
GA-10645	February 1, 1971 through April 30, 1971
GA-A10803	May 1, 1971 through July 31, 1971
GA-A10906	August 1, 1971 through October 31, 1971
GA-A12003	November 1, 1971 through January 31, 1972
GA-A12165	February 1, 1972 through April 30, 1972
GA-A12252	May 1, 1972 through July 31, 1972
GA-A12421	August 1, 1972 through October 31, 1972
GA-A12530	November 1, 1972 through January 31, 1973

ABSTRACT

The tasks of the Gas-Cooled Fast Breeder Reactor (GCFR) program that are supported by the U.S. Atomic Energy Commission are program planning, core development, development of a pressure equalization system for fuel rods, fuels and materials development, and nuclear analysis and reactor physics. Core development work included thermal-hydraulic analyses of the fuel-rod assembly, structural analyses of the fuel-rod spacer grid support and of the blanket-element box wall, construction of the fuel-rod–spacer interaction test apparatus, and development of a calculation model to predict fuel-rod behavior. The status of the GCFR thermal- and fast-flux irradiation programs is given. The results to date of the analyses of fission-gas release data from the vented-fuel-rod GB-10 being irradiated in the ORR and of the fast-flux F-1 experiment are given. Reactor physics work was concerned with surveillance of LMFBR critical assembly experiments, comparison of GGA and ANL calculational methods for critical assembly analysis, and defining goals and requirements for GCFR critical experiments program.

CONTENTS

Figures

Tables

1. INTRODUCTION

The Gas-Cooled Fast Breeder Reactor (GCFR) program sponsored by the U.S. Atomic Energy Commission consists of five tasks: Task 1000—Program Planning, Task 4100—Core Development, Task 4160—Pressure Equalization System for Fuel, Task 4200/4400—Fuels and Materials Development, and Task 4700—Nuclear Analysis and Reactor Physics. The broad objectives of each of these tasks and a summary of the work done on each task during the period covered by this report are given in this section. The work performed under each of these tasks during this reporting period is presented in Sections 2 through 6.

The GCFR Utility Program, which is supported by a large number of electric utility companies, rural electric cooperatives, and Gulf General Atomic, is primarily directed toward the development of a 300-MW(e) GCFR demonstration plant. This utility-sponsored work and the AEC-sponsored work are complementary.

1.1. TASK 1000—PROGRAM PLANNING

Work on this task is primarily directed toward implementing the technical development of the GCFR concept. This task also includes liaison with Argonne National Laboratory (ANL) and Oak Ridge National Laboratory (ORNL) on tasks they are performing under AEC funding; the corresponding work at Gulf General Atomic is being privately funded.

1.2. TASK 4100—CORE DEVELOPMENT

The objective of this task is the engineering development of the reactor core and associated components. The various investigations carried out under this task during this reporting period are given in Section 3.

Analytical studies of the fuel-element assembly are directed toward establishing design criteria for the development of the elements. Thermal-hydraulic and structural analyses made during this reporting period included (1) continuation of the investigations on the effects of fuel-rod displacement, particularly rod bowing; (2) the interaction of thermal-hydraulic effects and structural effects to establish temperature distributions at various time intervals during the life of the fuel element; (3) correlation of predicted thermal-hydraulic performance with experimental results; (4) a structural analysis of the reference-design support hanger for the fuel-rod spacer grids; and (5) initiation of an evaluation of the effects of thermal and mechanical loads, together with irradiation-induced swelling and creep, on distortion of the blanket-element box wall. The progress of the experimental program to evaluate the mechanical interaction between the spacer-grid dimple and the fuel-rod cladding surface is also given.

Modeling of the fuel and blanket rods is being made using the LIFE II code to develop a technique for predicting GCFR rod behavior. The results of the fast and thermal irradiations of GCFR fuel rods will be used to test the calculated predictions.

In the studies of the lower shield assembly, the investigation of the feasibility of removing heat from the top surface of debris in the lower shield assembly considered the reference reactor coolant system and an alternative reactor coolant system, pressurized and depressurized coolant loop conditions, and forced or natural circulation of the primary coolant gas.

1.3. TASK 4160—PRESSURE EQUALIZATION SYSTEM FOR FUEL

The objective of this task is to develop a system for equalizing the pressure between the inside and the outside of the GCFR fuel rod.

During this quarterly period, supplemental information on the development planning document for the GCFR pressure equalization system (PES) was prepared and submitted to the Division of Reactor Development and Technology for review.

1.4. TASK 4200/4400—FUELS AND MATERIALS DEVELOPMENT

The fuels and materials development and testing program extends and applies Liquid-metal Fast Breeder Reactor (LMFBR) fuel technology to GCFR requirements. This includes surveillance of the LMFBR fuels and materials program to utilize existing and developing technology applicable to the GCFR. The status of the GCFR thermal-flux and fast-flux irradiation test programs is presented in Section 5.

No further postirradiation examination of the GB-9 fuel rod was carried out at Argonne National Laboratory (ANL) during this period.

The vented-fuel-rod, sweep-gas capsule irradiation experiment GB-10, which is operating at 12 kW/ft and a maximum cladding temperature of 565°C, had reached a burnup of ~20,000 MWd/Te at the end of this reporting period. A comparison has been made of the calculated and measured release of radioactive fission gases from the solid oxide fuel matrix of GB-10 and analyses have been made of the relative transport delay times in the various parts of the fuel rod, of the release of activity on initial startup, and the results of leaking-rod simulation tests.

The seven encapsulated fuel rods in the F-1 (X094A) experiment are being subjected to a second interim examination after burnup exposures up to 56,000 MWd/Te were reached in the EBR-II. Five of the fuel-rod capsules will be removed during this interim examination and replaced with five unirradiated fuel rods.

Leak tests were made of the seven F-1 fuel rods and all of the rods appeared to be intact. Selected regions of the fuel rods in three of the capsules were precision gamma scanned, and from a preliminary analysis, no unusual behavior was indicated.

Postirradiation examination of capsule G-3, which was removed from the F-1 experiment during the first interim examination after a burnup exposure of ~27,000 MWd/Te, included flow tests through the fuel rod, optical microscopy of five fuel-rod samples to determine the extent of grain boundary attack at the fuel-cladding interface, and examination of longitudinal sections taken at the top and bottom of the fuel column.

Preparations for the fast-flux experiment F-3 continued. The final capsule design drawings were sent to ANL and the EBR-II Project and the fuel-rod hardware was shipped to ANL for loading and assembly into the fuel-rod capsules.

1.5. TASK 4700—NUCLEAR ANALYSIS AND REACTOR PHYSICS

This task involves the surveillance of LMFBR physics work and critical experiments to properly coordinate and develop a complementary GCFR nuclear analysis and physics program. The work performed under this task during this reporting period is discussed in Section 6.

Surveillance of LMFBR critical assembly experiments continued with the objective of establishing an experimentally verified basis for GCFR reactor physics work. A comparison of GGA and ANL calculation methods was started for selected reactor physics parameters for the sodium-flooded and sodium-voided ZPR-6 Assembly 6-A. Also, work continued on the definition of goals and requirements of a GCFR critical experiments program.

2. TASK 1000—PROGRAM PLANNING

The preparation of a quality assurance program for the GCFR project was the only work performed under this task during this period.

3. TASK 4100—CORE DEVELOPMENT

3.1. FUEL-ELEMENT ASSEMBLY

The work on obtaining information for establishing design criteria for development of the fuel-element assemblies was continued. The factors affecting the design criteria of the assembly were summarized in a previous quarterly report.[1] The analytical work that was previously reported[1,2] treated the initial thermal-hydraulic behavior of the fuel-rod bundle by the use of the HETHRA code (a revision of the COBRA II code) described in Ref. 2, and separately treated the structural distortion of the fuel rods with the CRASIB code.[3] This approach led to an understanding of the sensitivity of the thermal-hydraulic performance of the rod bundle to fuel-rod distortions as predicted by CRASIB. During the current reporting period,

1. Studies of the effects of rod bowing were continued to the point where adjacent rods approached touching,
2. An iterative approach was introduced in which the effects of the rod displacement were coupled with the thermal-hydraulic analysis to establish new temperature distributions at various time intervals during the fuel-element lifetime, and
3. The results of analyses using the thermal-hydraulic code HETHRA were verified by comparison with experimental data.

Previously reported structural analyses and experimental measurements on the stiffness of the rod spacer grid and the spacer-grid dimple were extended to the spacer support hanger. In addition, analyses were initiated to evaluate the effects of thermal and mechanical loads, together with irradiation-induced swelling and creep, on distortion of the blanket-element box wall.

Construction of the test apparatus for measuring spacer-rod interactions as a function of helium purity, operating conditions, and spacer geometry is nearing completion.

3.1.1. Thermal-Hydraulic Analyses

3.1.1.1. Rod Displacement Effects. The thermal-hydraulic effects of uniform rod displacement were studied previously.[2] This analysis was continued to study the results of fuel-rod bowing up to the point where adjacent rods approached touching. Bowing rather than uniform displacement is considered because it provides a better description of the fuel-rod behavior between the spacers. The cladding and coolant temperature distributions were determined for a 7-rod bundle with uniform heating where the center rod was bowed sinusoidally. The results are given below.

Center-rod Bowing (mils)	Minimum Clearance (mils)	Maximum Cladding Temperature (°F)	Temperature Gradient Across Rod		
			At Position of Minimum Clearance (°F)	At Position of Maximum Gradient (°F)	At Bundle Outlet (°F)
0	104	1106	0	0	0
25	79	1117	25	37	21
50	54	1127	47	72	43
75	29	1136	75	108	60
100	4	1143	79	153	75

The maximum cladding temperature does not occur at the minimum clearance location but at a point downstream. The restriction reduces the coolant flow in the affected subchannels, which causes an above-average coolant temperature rise that continues to increase even beyond the minimum clearance location. Eventually, the coolant flow increases locally and transverse mixing of the coolant causes the local coolant temperature to rise and again approach the average temperature rise. Also, the reduced flow causes an increase in the heat-transfer temperature difference. This behavior is reflected in the temperature gradient values where the temperature gradients at the bundle outlet are less than the temperature gradients upstream. The maximum bowing displacements are conservatively much larger than the displacements calculated in the structural analysis of the fuel rod. It is noted that the maximum cladding temperatures are below the design limit of 700°C (1292°F). The analytical model includes flow redistribution but neglects local variation of

the heat-transfer coefficient over a subchannel, which is nonconservative. However, conduction within the fuel rod and cladding is neglected, which is conservative. It is estimated that the net result of the neglected phenomena would not cause an error in cladding temperature of more than 50°F.

3.1.1.2. Interaction of Thermal-Hydraulic and Structural Effects. The fuel-rod–spacer interaction is coupled to the structural behavior of the fuel rods, which, in turn, is coupled to the thermal-hydraulic performance of the fuel element. Qualitatively, the interaction may be described as follows: (1) Within a fuel element, even for nominal conditions, radial temperature gradients are produced because of nonuniform flow and radial power variation (power tilt); (2) the radial temperature gradients induce differential thermal expansion, which causes fuel-rod bending; (3) as the end of operational life of a fuel element is approached, additional differential expansion caused by the neutron-fluence-induced swelling results in further rod bending; (4) the bending is restricted by the fuel-rod spacers but bending does occur between spacers; (5) the rod bending distorts the coolant flow passages and changes the local coolant flow and fuel-cladding temperatures, which generally increase the radial temperature gradients; and (6) the increased radial temperature gradients cause increased differential expansion and thus an increase in rod bending.

An equilibrium condition will exist where the structural thermal-hydraulic interactions are balanced. A properly designed element will reach this equilibrium condition in which the maximum cladding temperature, cladding stress, and spacer loading remain below the design limits. An analysis has been made to determine the maximum cladding temperature, maximum cladding stress, and maximum spacer loading at a position in the GCFR reference core and at the operating time when these quantities are expected to be at a maximum.

The maximum radial neutron flux gradient and the maximum radial power gradient occur in the outer ring of core elements. Within these elements, the maximum cladding temperature and maximum neutron fluence occur in the region of maximum neutron flux. Thus, an outer core element was chosen for the analysis and the region within this element was where the neutron flux would be at a maximum. Radiation-induced swelling is dependent on the

neutron fluence that reaches a maximum at the end of operational life for a fuel element and the fuel-rod bending and distortion are assumed to be a maximum at this time; therefore, the analysis was centered on the end of fuel element life to generate maximum values of temperatures, stresses, and loads. The end-of-life temperature distribution was assumed during the entire time-dependent calculation with the CRASIB code. Another conservative simplifying assumption was that periodic element rotation in the reference design to reduce distortion was neglected. Based on the physics data of Ref. 4, the power and neutron flux (< 0.1 MeV) for the element chosen are given in Table 3.1 and the detailed relative power distribution is shown in Fig. 3.1 for the maximum power region for that element.

The end-of-life performance of the element was determined by the following iterative process:

1. A thermal analysis (HETHRA) of the outer-ring fuel element with nominal geometry to generate axial and radial cladding temperatures.
2. A structural analysis (CRASIB) using as input the thermal information to generate distorted geometry of fuel rods and coolant passages.
3. A thermal analysis (HETHRA) with distorted geometry to generate axial and radial cladding temperatures for the distorted geometry.
4. An iteration to obtain the converged solution to the thermal-hydraulic-structural interaction.

The converged solution was determined with fewer calculations by an increase in the thermal analysis results of (1). The thermal results were used in (2) and the results of (3) were checked to ascertain that they do not exceed the adjusted input from (1).

In the thermal-hydraulic analysis, the region of maximum power was approximated by a 37-rod bundle since a previous analysis of this configuration had shown that local distortion effects do not propagate farther than two rows of rods. The dimensions and operating conditions for the GCFR reference design were used in the calculation of temperatures for the nominal geometry. The fuel-rod cladding is roughened over three-fourths of

Table 3.1

POWER AND NEUTRON FLUX FOR OUTER-RING ELEMENT

Operating Time (Full power days)	Location in Element[a]						
	1	2	3	4	5	6	7
Power Ratio (Local/Core Average)							
0 (startup)	0.809	1.009	1.189	1.197	1.031	0.837	1.029
250 (shutdown)	0.818	1.013	1.185	1.193	1.034	0.846	1.032
250 (restart)	0.773	0.957	1.127	1.137	0.982	0.803	0.978
500 (shutdown)	0.785	0.964	1.127	1.135	0.987	0.814	0.983
500 (restart)	0.725	0.901	1.066	1.078	0.934	0.760	0.922
750 (end of life)	0.739	0.910	1.069	1.081	0.942	0.773	0.931
Values used for calculation	0.751	0.943	1.121	1.132	0.972	0.784	0.964
Core Mid-plane Neutron Flux ($n/cm^2/sec$ (> 0.1 MeV) x 10^{-15})							
0	1.44	1.80	2.12	2.14	1.84	1.49	1.84
250	1.51	1.86	2.18	2.20	1.90	1.56	1.90
250	1.44	1.79	2.11	2.12	1.83	1.50	1.83
500	1.51	1.85	2.16	2.18	1.89	1.56	1.89
500	1.41	1.75	2.07	2.09	1.81	1.47	1.79
750	1.47	1.81	2.12	2.15	1.87	1.54	1.85
Values used for calculation	1.51	1.86	2.18	2.20	1.90	1.56	1.90

[a]Locations in element are:

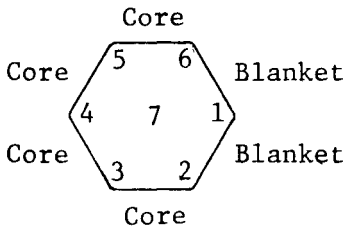

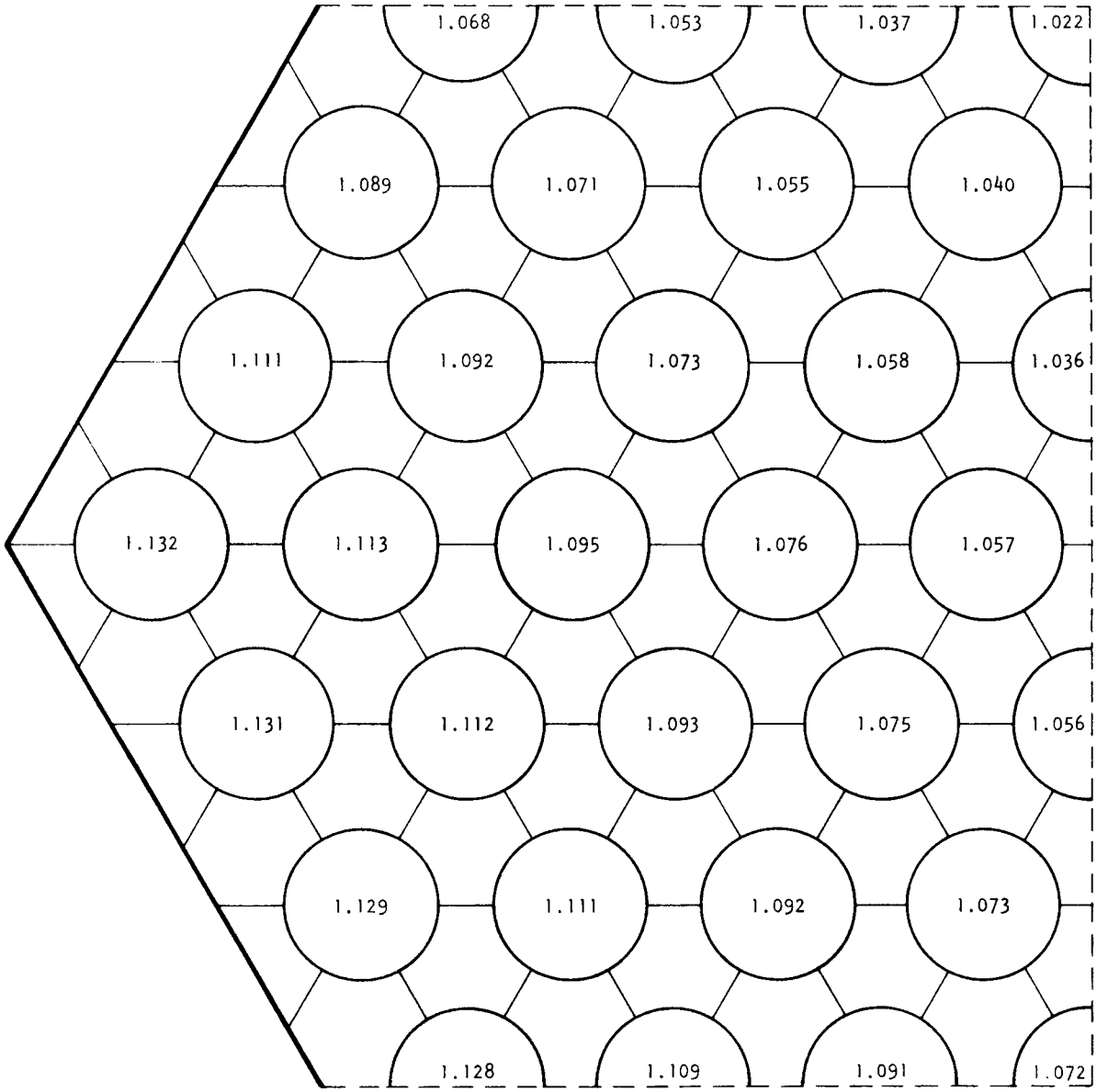

Fig. 3.1 Detailed relative power of outer-ring core element showing maximum values during fuel cycle (relative power = (local power/core average power) at midplane)

the active rod length and the spacer support hanger in the element is assumed to be corrugated to obtain near optimum flow in the region near the element wall. The axial power distribution is a chopped cosine through the core; blanket power is considered negligible. The maximum wall temperatures occur at about 90% of the axial distance through the core. Figure 3.2 shows the coolant temperatures and the cladding surface temperatures at the axial position of maximum surface temperature with nominal geometry. The subchannels that will have increased temperature due to rod bowing are assumed to be on the hot side of the temperature gradient in the surrounding rods, and, ideally, a rod will bow in the direction of the hotter side. The cross-hatched subchannel in Fig. 3.2 is surrounded by fuel rods with their hottest side facing this subchannel. Therefore, this subchannel is expected to have the maximum reduction of flow area and the corresponding greatest increase in temperature when distortion is considered. It may be noted that the maximum cladding surface temperature is in fuel rod A, located at the left-hand corner of this subchannel, but a design change, such as increasing the rod-to-corner clearance by reducing the corner rod diameter or reducing rod power by changing fuel loading, would eliminate this higher temperature. The temperature profiles for the fuel rods labeled A, B, and C in Fig. 3.2 were used as input data for the distortion calculation.

The structural analysis of the three fuel rods was performed using the CRASIB code. The operating conditions used were the axial temperature, axial neutron fluxes, linear temperature gradients, and linear flux gradients. As the code is presently set up, the temperature and neutron-flux gradients must be in the same transverse direction. From the thermal analysis, the temperatures calculated for the nominal geometry are not linear in a transverse direction, and the calculated peak values are also conservatively high because circumferential conduction around the fuel rod is negelected. The temperature gradients were thus calculated on the basis of the maximum surface temperatures in the transverse direction of interest. The neutron flux gradient was assumed to be in the same direction as the temperature gradient so that the bending caused by temperature and radiation swelling will be in the same direction. This is an assumption that will cause an overestimate of the temperature increase caused by distortion.

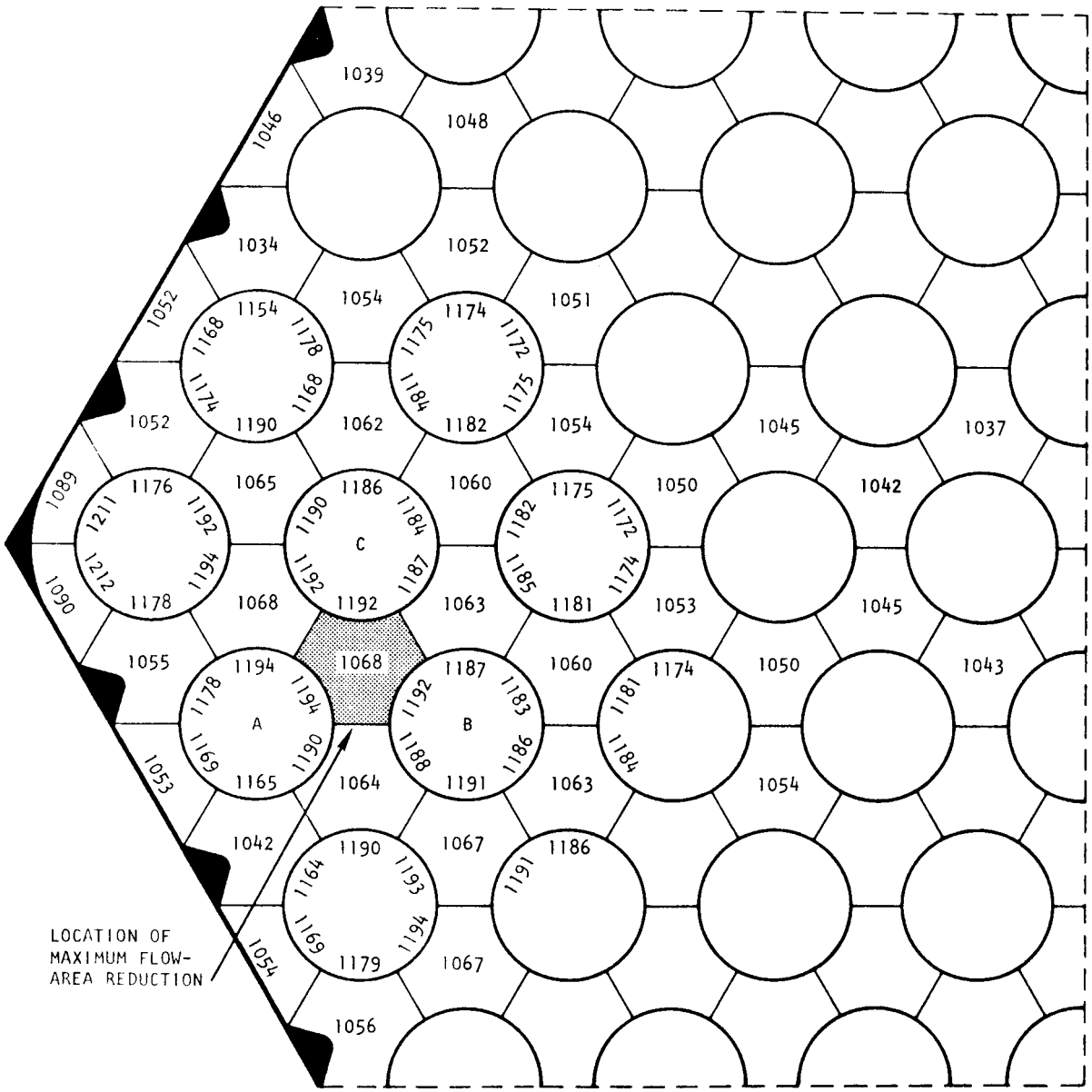

Fig. 3.2 Coolant and cladding surface temperatures at axial position of maximum surface temperature for nominal geometry

After iterating, distortion is computed to increase the temperature gradient across rod A by a factor of 1.5 and across rods B and C by a factor of 2.4. The calculated distortions for the end of operating life are shown in Fig. 3.3 for rod A and in Fig. 3.4 for rods B and C using the above multiplying factors. The fuel rods are fixed at the spacer location but are allowed to distort between spacers. The fine structure of the displacement shows that the flow subchannel of interest will be both restricted and expanded over the axial length. To be on the conservative side, the displacement was approximated by assuming the maximum displacement from the core inlet to the reactor outlet to be in the direction of restricting the subchannel. For fuel rods B and C, the displacement downstream of the core is ignored since the axial blanket at the outlet will not affect the maximum cladding surface temperature.

The thermal-hydraulic calculation was repeated with modified axial subchannel values to account for the rod bowing. At the core inlet, rods A, B, and C moved toward each other, which restricted the subchannel between them and expanded the subchannel on the opposite side of each rod. These subchannel changes were assumed constant from the core inlet to the reactor outlet. Figure 3.5 shows the cladding surface and coolant temperatures at the axial position where the cladding surface temperatures are a maximum near the core outlet. This is a conservative calculation of the cladding surface temperatures at end of life to account for the effect of fuel-rod distortion. A comparison of the temperatures for nominal geometry and distorted geometry are given in Table 3.2.

Table 3.2

CLADDING SURFACE TEMPERATURES FOR NOMINAL AND DISTORTED ELEMENTS

	No Distortion			End-of-life Distortion		
Region	Maximum Temp. (°F)	Minimum Temp. (°F)	ΔT/R	Maximum Temp. (°F)	Minimum Temp. (°F)	ΔT/R
Fuel rod A	1194	1169	88°F/in.	1199	1162	130°F/in.
Fuel rod B	1192	1186	21°F/in.	1196	1186	35°F/in.
Fuel rod C	1192	1186	21°F/in.	1197	1186	39°F/in.
Coolant		1086			1072	

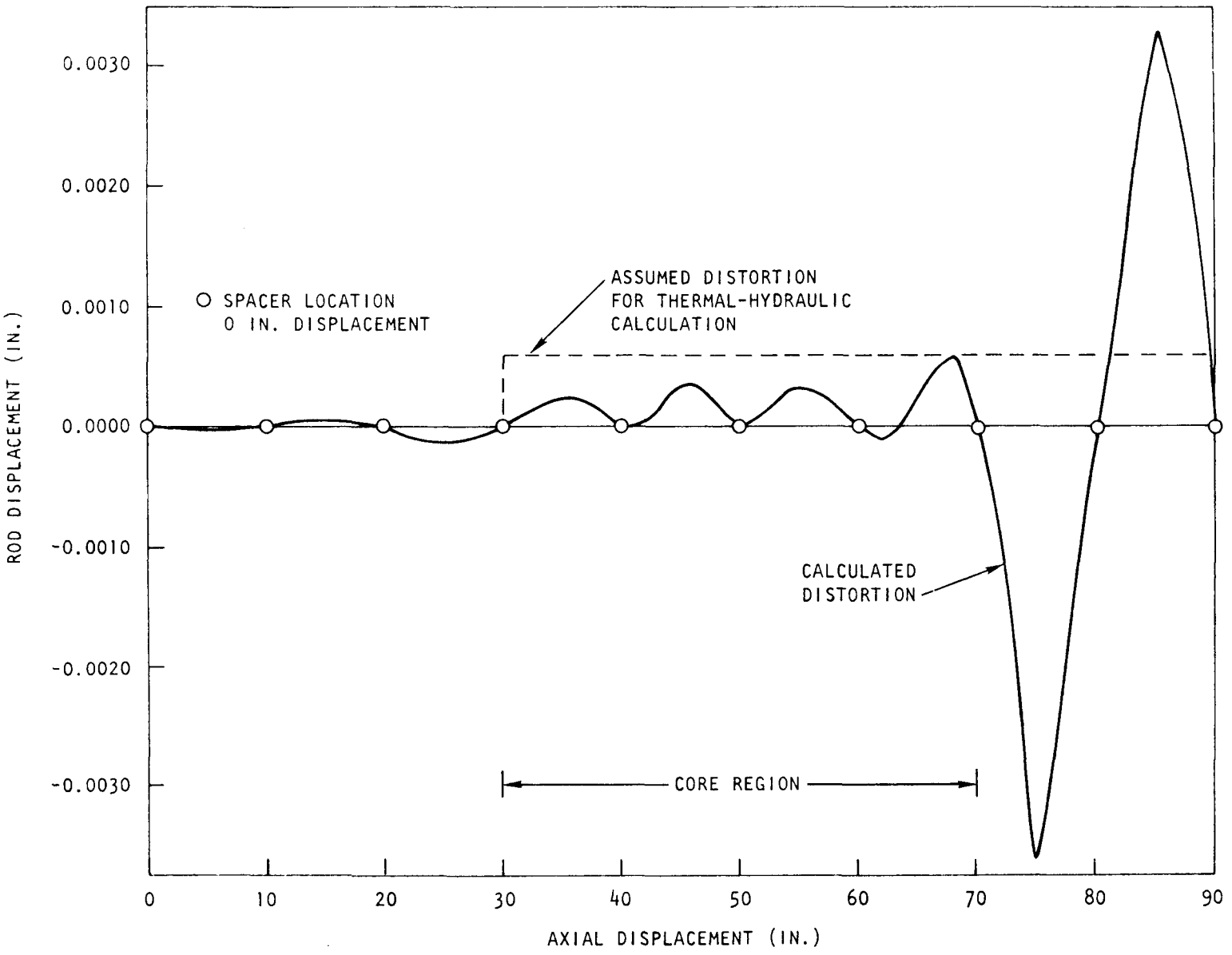

Fig. 3.3 Calculated distortion for rod A (see Fig. 3.2) in outer-ring core element

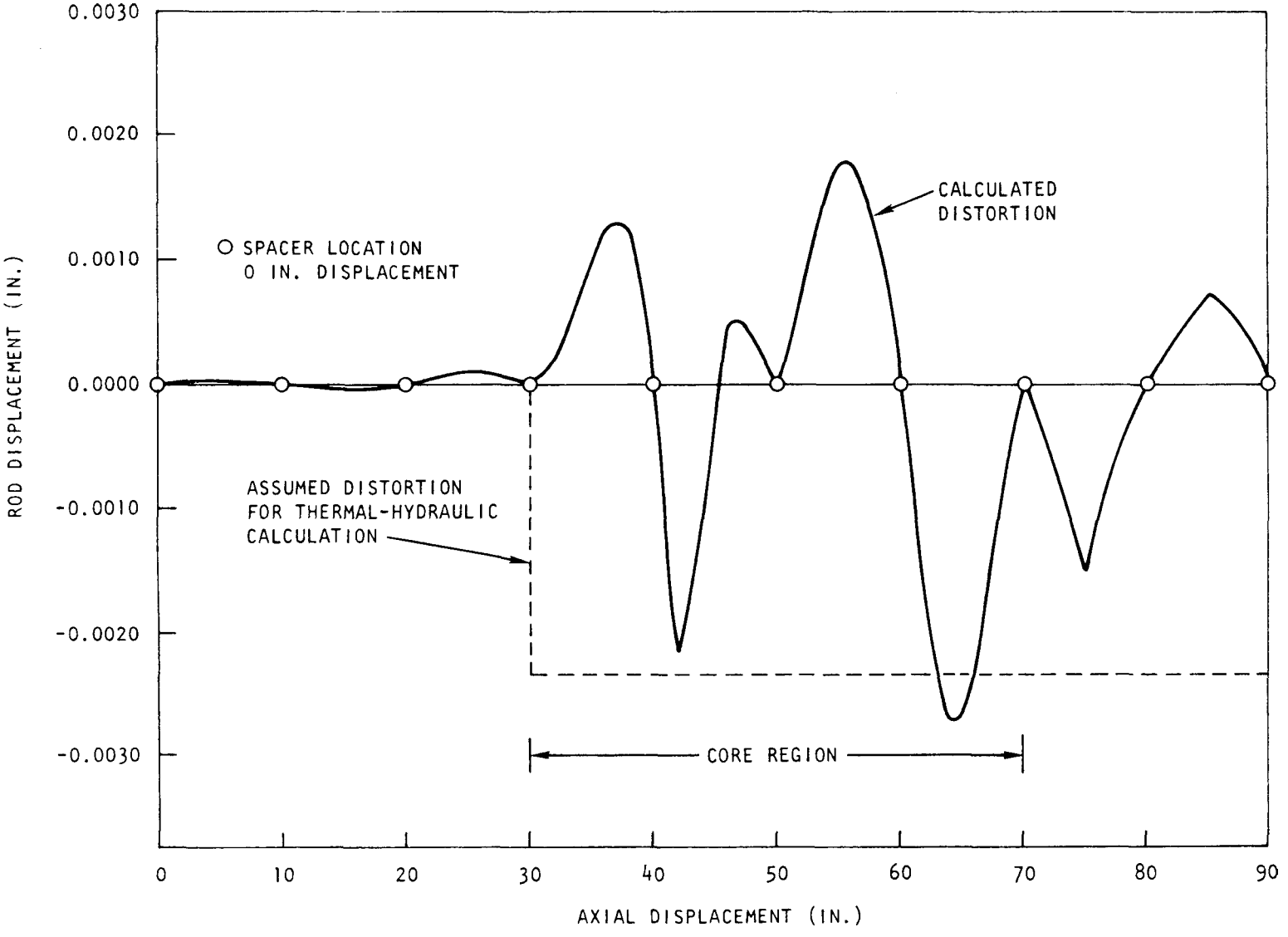

Fig. 3.4 Calculated distortion for rods B and C (see Fig. 3.2) in outer-ring core element

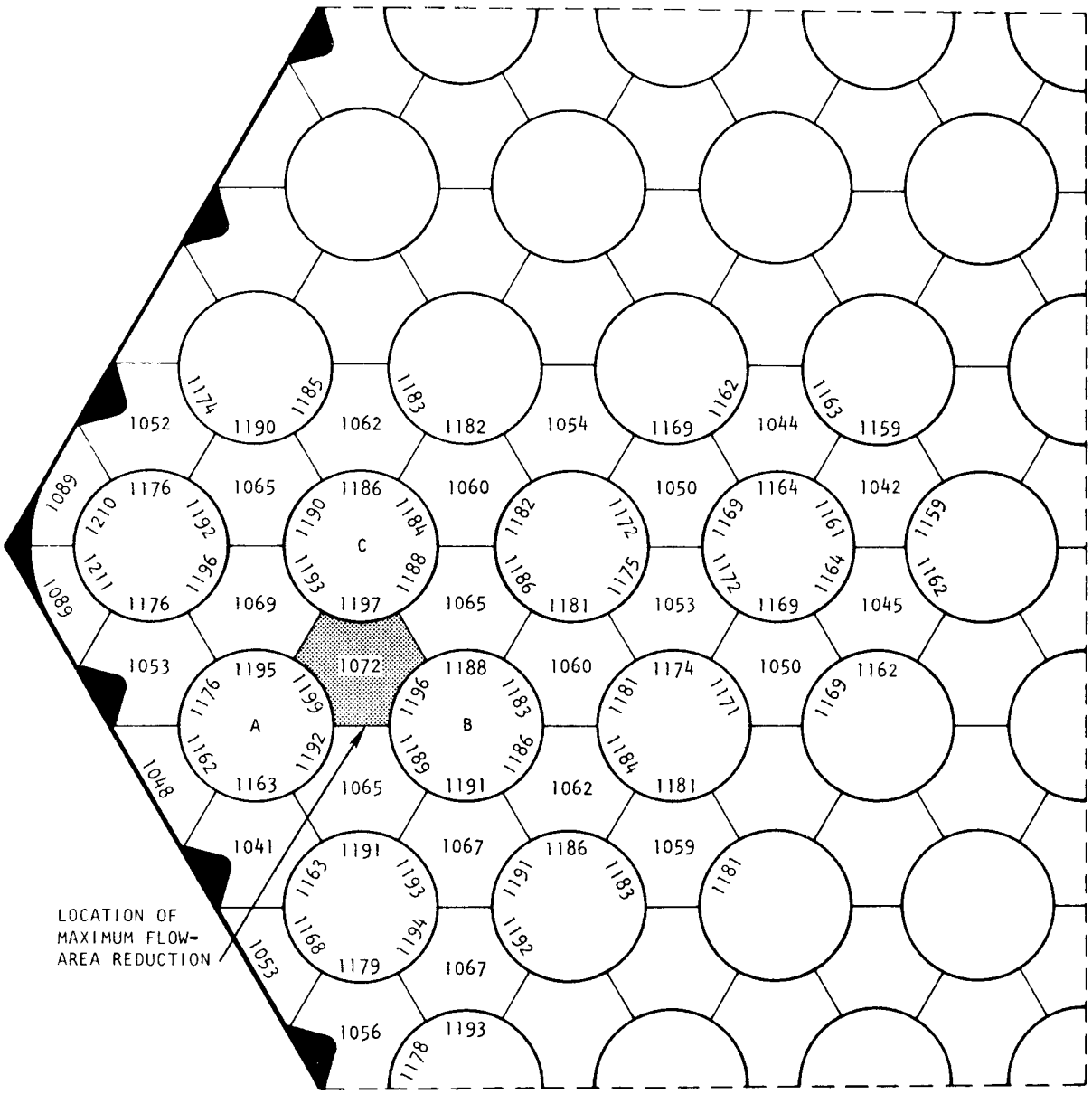

Fig. 3.5 Coolant and cladding surface temperatures at axial position of maximum surface temperature for distorted geometry

The analysis indicated that the temperature changes caused by distortion are small and that the design is satisfactory since the cladding surface temperature is approximately 90°F below the design limit of 1292°F. The interaction of thermal-hydraulic structural factors and radiation swelling are not significant enough to cause a substantial rise in the cladding surface temperature.

3.1.1.3. Correlation of the Thermal-Hydraulic Analysis with Experiment. The results of the thermal-hydraulic analysis using HETHRA were verified by comparing them with experimental data from two heat-transfer tests. The experiment consisted of 19 heated rods in a circular element that was cooled by carbon dioxide. These tests were performed under a privately sponsored program.

3.1.2. Structural Analyses

3.1.2.1. Fuel-element Box Wall Distortion. In the analysis of the fuel-element box wall, a complex three-dimensional state of stress and strain is assumed to be represented by the more readily understood states of generalized plane strain or plane stress. This essentially uncouples a thin horizontal slice of the box wall from parallel slices above and below it and reduces the three-dimensional problem to a two-dimensional problem. The generalized plane strain case may be analyzed by a finite-element code, but, unfortunately, it requires a large number of finite elements to adequately represent the geometry of the box wall and is expensive to run. Therefore, a general plane-strain structural analysis of the hexagonal fuel-element box wall was attempted using an existing finite-element code that was modified to include the effects of irradiation swelling and creep correlation. However, the elastic stresses predicted by the code (8,000 psi) are only about 66% of those calculated by hand using simple elastic beam theory (12,000 psi). The approximation of the box-wall elements as simple beams is not accurate and one would expect higher stress predictions from the simple beam model. However, the elastic stress in an element of the box wall should be within about 85% of the simple beam model for the same loading. The reason for the lack of agreement on the elastic analysis is being investigated.

An alternative approach is to use a code such as CRASIB[3] which uncouples the horizontal slice from neighboring slices and the slice is assumed to be in a state of plane stress. This stress state is further simplified to a one-dimensional state of stress since the box wall is thin and thus the transverse stress is small and assumed to be zero. The CRASIB code was modified so that it could be used to analyze the thin horizontal slice as a segmented beam with a width of unity along the long axis of the fuel element and a beam depth equal to the box wall thickness. This approach requires the beam-element stiffnesses to be rotated by the appropriate amount as the beam proceeds to bend at the box wall corners. Furthermore, the imposed thermal and flux gradients must be altered for the rotated beam elements. Also included in the modification is a transformation in the stiffness matrix of the code to include the beam geometry simulated by the box wall. Calculations using this modified code are being initiated.

From the standpoint of computer costs and accuracy of the displacement field for cases involving many time steps to lifetimes of 20,000 hr, the modified CRASIB approach is better. If the solutions are satisfactory, then future calculations will be accomplished with the modified CRASIB code.

3.1.2.2. Spacer Support Hanger. The GCFR reference design fuel element assembly includes 8 honeycomb fuel-rod spacers that are ~9.75 in. apart along the length of the rods starting from the upper fuel-rod support grid. Each spacer is supported by six 8-in.-long vertical plates, or hangers. The lower end of the support plate is welded to the outer edge of the spacer and the upper end is welded to the element box wall. The principal design function of the support plate is to provide for differential expansions and displacement between the spacer and the element box wall. Each of these plates acts as a low-stress spring that allows differential movement of the walls and the spacer grid. Thus, the spacer grid will be decoupled from the loading due to distortion of the element box wall. An additional function of the support plates is to act as a flow shroud around the outer row of fuel rods. For this purpose, the plates are corrugated, or fluted, in cross section (see Fig. 3.6). The corrugated cross section of the support plate

changes to a flat cross section at the upper end so that the plate can be welded to the box wall.

In the design evaluation of the fuel-element assembly, several questions have arisen concerning these spacer support hangers, such as

1. Is the corrugated cross section necessary for flow shrouding of the outer row of rods?
2. How long do the support plates have to be?

The answer to the first question is being determined in the thermal-hydraulic analysis. A review of the FFTF grid-type sodium-cooled fuel element assembly drawings in Refs. 5 and 6 indicates that a flow shroud for the coolant will not be included because the support plate in the FFTF element is a flat strap. However, the thermal-hydraulic calculations carried out for the GCFR element reference design indicate that there is an advantage to having a flow shroud for the outer row of rods with the use of helium coolant.

The answer to the second question depends on two considerations. The first is whether the corrugated coolant shroud is necessary and, second, the amount of flexibility necessary to isolate the fuel-rod support grid and outer flow channels from the effects of box wall distortion and loading. If it is assumed that a corrugated flow shroud is necessary, then the hangers must extend the distance between the support grids, or ~9.75 in. Calculation of the spring constant of the spacer support hanger would be somewhat complicated and would have a large uncertainty because of the corrugated cross section. To determine the effective moment of inertia, the spring constant of a corrugated support hanger was measured by cantilevering a 4-in.-long section and loading it as shown in Fig. 3.6. The value of the spring constant at room temperature was 25.5 lb/in. for the 4-in. beam length. The moment of inertia is obtained from the following general equation for a cantilevered beam loaded at one end:

$$y = -\frac{1}{3}\frac{W\ell^3}{EI} \quad \text{(from Case 1, Table III of Ref. 7).} \qquad (1)$$

where y = deflection (in.),

W = load (lb/in.),

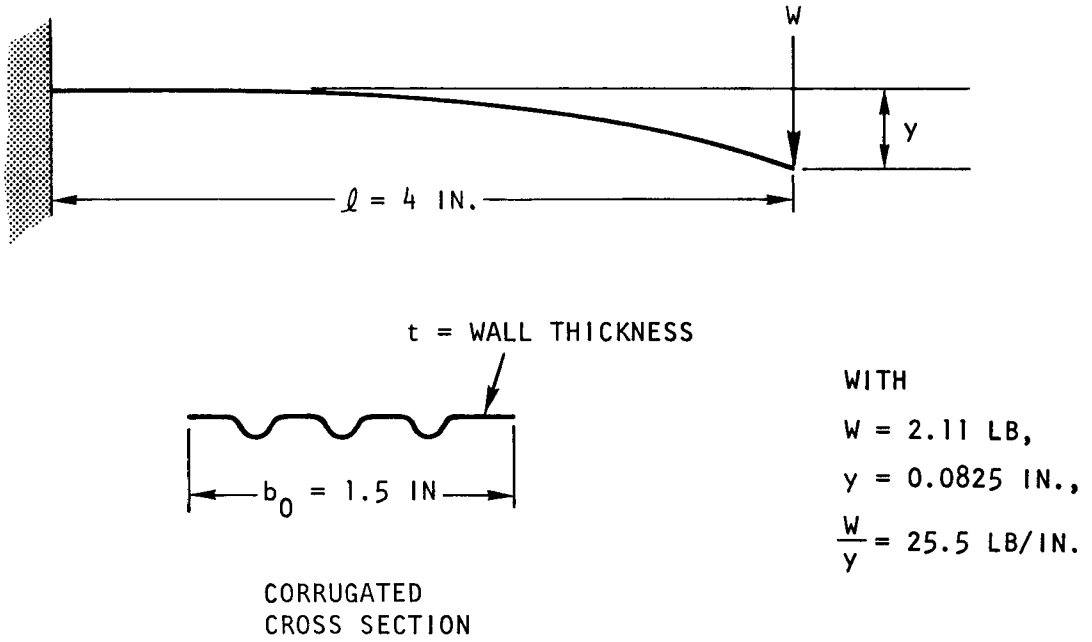

Fig. 3.6 Schematic of a corrugated spacer support hanger tested as a cantilevered beam

ℓ = hanger length (in.),

E = Young's modulus,

I = moment of inertia,

and the effective moment of inertia, I_0, is

$$I_0 = -\frac{W\ell_0^3}{y_0\ 3E_0} . \qquad (2)$$

Then, with

ℓ_0 = 4 in.,

E_0 = 28 x 10^6 psi for SA Type 316 stainless steel,

$\left(\frac{W}{y}\right)_0$ = 25.5 lb/in.

and substituting these values in Eq. (2), the effective moment of inertia is

$$I_0 = -\frac{(4)^3 \times 25.5}{3 \times 28 \times 10^6} = 1.94 \times 10^{-5} \text{ in.}^4 .$$

The effective spring constant for the GCFR reference spacer design can be estimated by correcting the modulus E for operating temperature and correcting for the width, b, of the support hanger (3.75 in. for the reference design versus 1.5 in. for the test specimen). Thus,

$$I = I_0 \left(\frac{b}{b_0}\right), \qquad \text{with } \frac{b}{b_0} = \frac{3.75}{1.5} = 2.5$$

and

$$\frac{W}{y} = \left(\frac{W}{y}\right)_0 \left(\frac{I}{I_0}\right)\left(\frac{E}{E_0}\right)\left(\frac{\ell_0}{\ell}\right)^3$$

where $E = 22 \times 10^6$ psi at 1100°F. Then,

$$\frac{W}{y} = 25.5 \left(\frac{3.75}{1.5}\right)\left(\frac{22}{28}\right)\left(\frac{4}{\ell}\right)^3$$

or

$$\frac{W}{y} = \frac{3200}{\ell^3} .$$

The spring constant as a function of support length is given in Fig. 3.7.

If a corrugated hanger or shroud are not required, a flat support hanger could be used and the moment of inertia is that of a rectangular area, or

$$I = \frac{bt^3}{12}$$

where b = section width = 3.6 in.,

t = section thickness = 0.025, 0.030, or 0.035 in.

The corresponding spring constants for a noncorrugated support hanger are also given in Fig. 3.7 as a function of wall thickness.

In addition to the flexure properties of the support hanger, the bending stress must be considered. The formula for the bending stress in a beam is

$$\sigma = \frac{MC}{I} .$$

For a corrugated section,

$$\frac{C}{I} = \frac{h + t}{2I}, \qquad \text{(from Ref. 7, pages 5 - 39)},$$

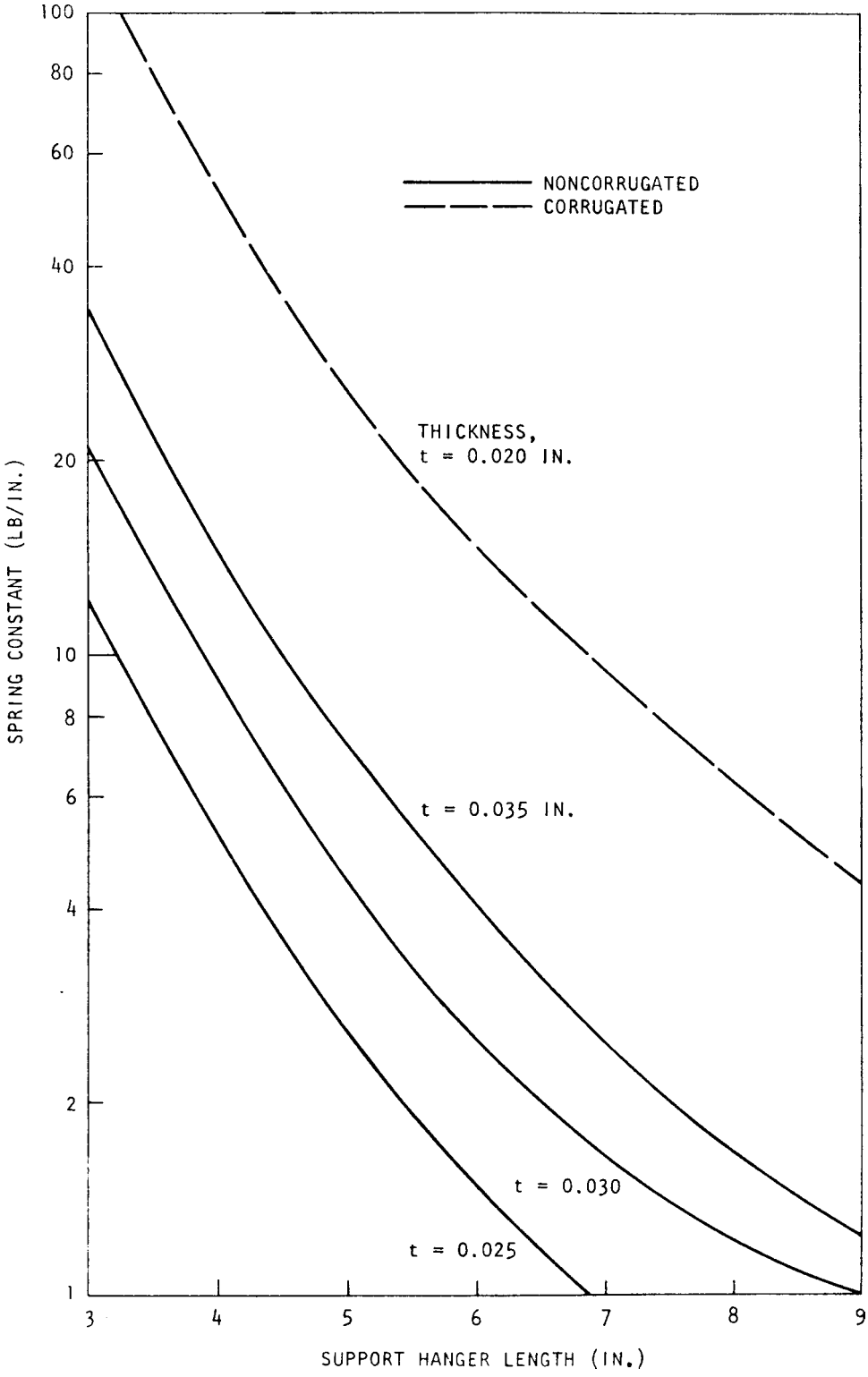

Fig. 3.7 Spring constant vs. length for corrugated and noncorrugated support hangers

where h = corrugation height = 0.108 in.,

t = wall thickness = 0.030 in.,

M = Wℓ (bending moment).

Therefore,

$$\sigma = \frac{W\ell(h + t)}{2I} .$$

With

$$I = \frac{W\ell^3}{y3E} \qquad \text{(from Eq. (2))},$$

$$\sigma = \frac{3Ey(h + t)}{2\ell^2} \quad \text{(for a corrugated support hanger)}$$

and

$$\sigma = \frac{3Eyt}{2\ell^2} \quad \text{(for a flat support hanger)}.$$

The elastic stress values are plotted as a function of hanger length for various deflection values, y, in Fig. 3.8. The deflections, y, would be due to bending of the element box wall where the support hanger is welded to the wall. A differential deflection as great as 0.150 in. would not be expected until the end of element life. Even at that time, the stresses would be low for an 8-in.-long corrugated hanger. The reaction loads are typically about 2 lb or less. If the corrugations are not necessary, then a flat hanger 3 to 4 in. long and 0.030 in. thick would provide adequate flexibility (W/y < 50 lb/in.) and would have low bending stresses (< 10,000 psi) at the end of life, as shown in Fig. 3.9.

3.1.3. Fuel-rod–Spacer Interaction Tests

The test objectives and mechanical design of the test apparatus were described in previous technical progress reports.[1,2] The work during the present quarterly period covered two areas: fabrication and assembly of the test apparatus and assembly and testing of the gas supply system and associated instrumentation.

The assembled apparatus is shown in Fig. 3.10. The drive system, cycle switches, and limit switches have been checked out and the load cells respond as expected in room-temperature cycling. One design change was

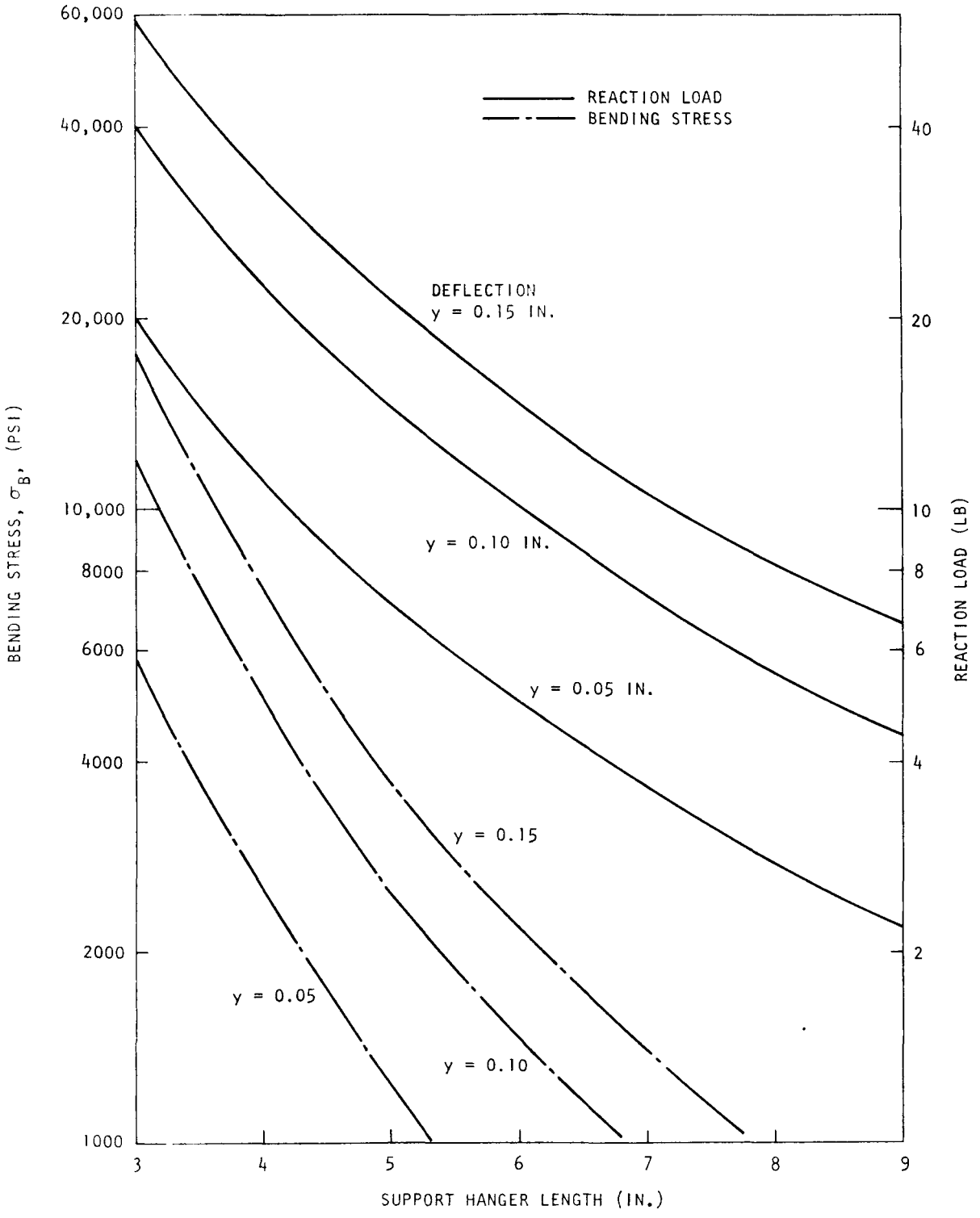

Fig. 3.8 Bending stresses and reaction loads on corrugated support hanger

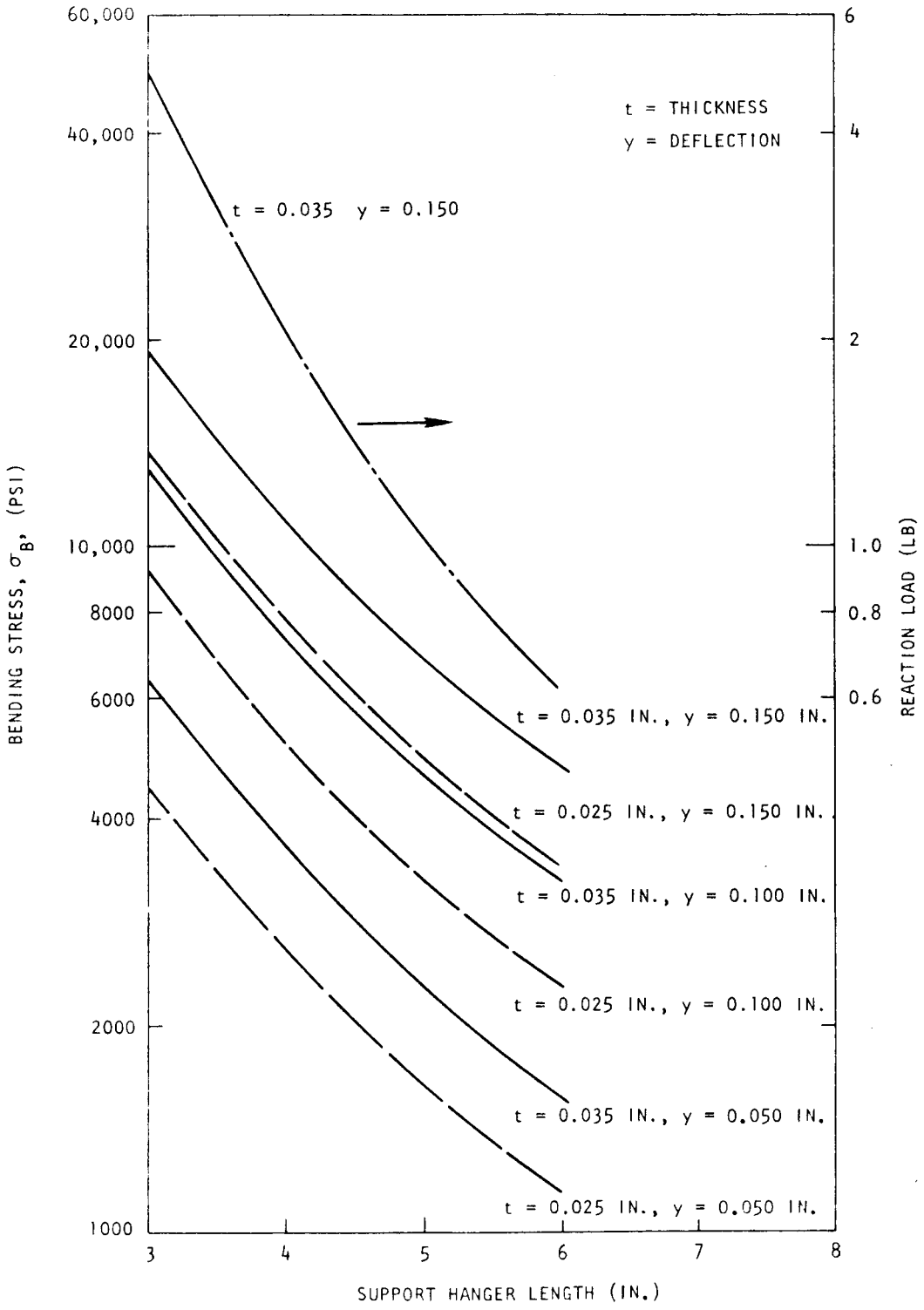

Fig. 3.9 Bending stresses and reaction loads on noncorrugated support hanger

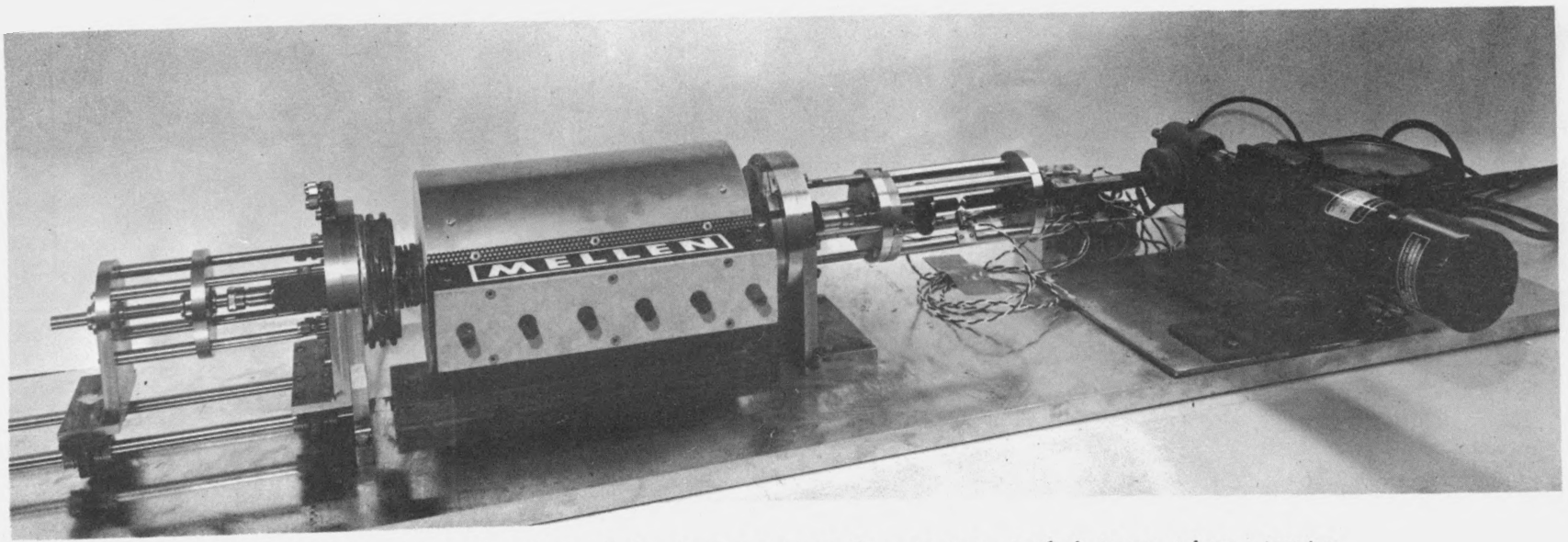

Fig. 3.10 Overall view of test apparatus for spacer-rod interaction tests

made, which was to replace the bellows loading on a single spacer cell with dead loading on two spacer cells that are about 1.25 in. apart. The axial load imparted to the spacers by the moving ribbed test rod is restrained by two rods connected to the load cells at the left-hand flange in Fig. 3.11. The error in load-cell reading due to angular deflection of the load rods, which was due to the downward motion of the spacer block and weight, is negligible because the test rod and drive rods are relatively stiff and allow little vertical deflection. The use of dead loading rather than loading with the gas-actuated bellows eliminated the need for a precise differential pressure controller to provide the proper gas pressure to the bellows and also eliminated the uncertainties in the spring rate of the various components as a function of temperature. The instrumentation to be used at this time consists of regulated power supplies for the load cells, strip chart recorders for the load cells, and a multipoint recorder for the temperature, flow rate, water content in the gas, and hydrogen-to-water ratio. In addition, a predetermining counter will be used to ensure that the desired number of test cycles will be performed.

The gas-control and analysis system was set up with instrumentation to monitor the water level in the supply gas and, after adding water to the gas stream, to monitor it again, and to measure the hydrogen-to-water ratio before and after adding additional water to the gas stream. (A schematic of this system is shown in Fig. 3.12.) The supply helium is obtained with known levels of hydrogen in the desired range. In the original design of the gas control scheme, the water impurity was generated by passing helium with a known hydrogen level through a hot copper oxide bed, which converted the hydrogen to water. The water level was measured with a Panametrics moisture monitor and the hydrogen-to-water ratio was measured directly by a Thermox meter. However, difficulties were encountered in maintaining complete conversion of hydrogen to water over long periods of time. An alternative moisture-generation system has been tested successfully and a final version is now being fabricated. This system, which has been tested previously at GGA, employs an ice trap held at a constant temperature to supply the proper moisture level to the helium-hydrogen mixture.

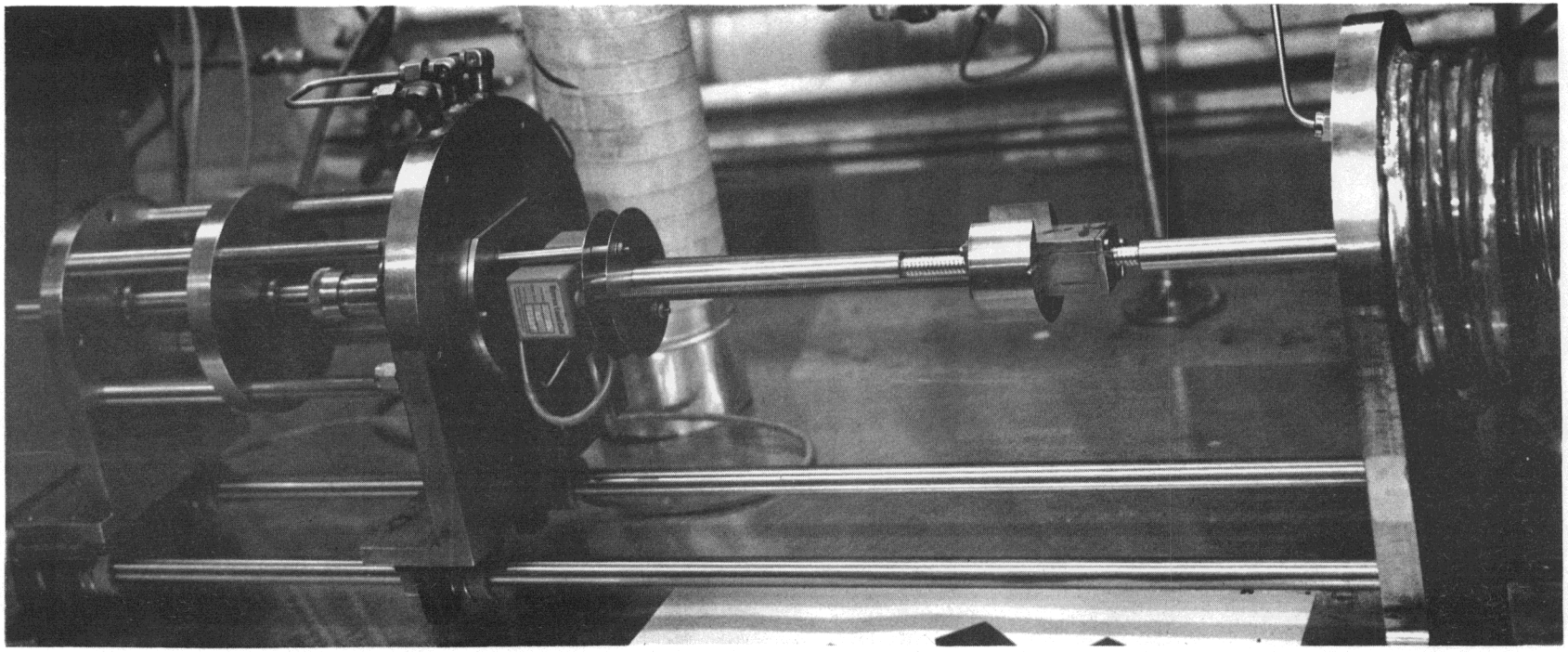

Fig. 3.11 View of interior parts of spacer-rod interaction test apparatus showing load cells, helically roughened tube sample, and dead weight load

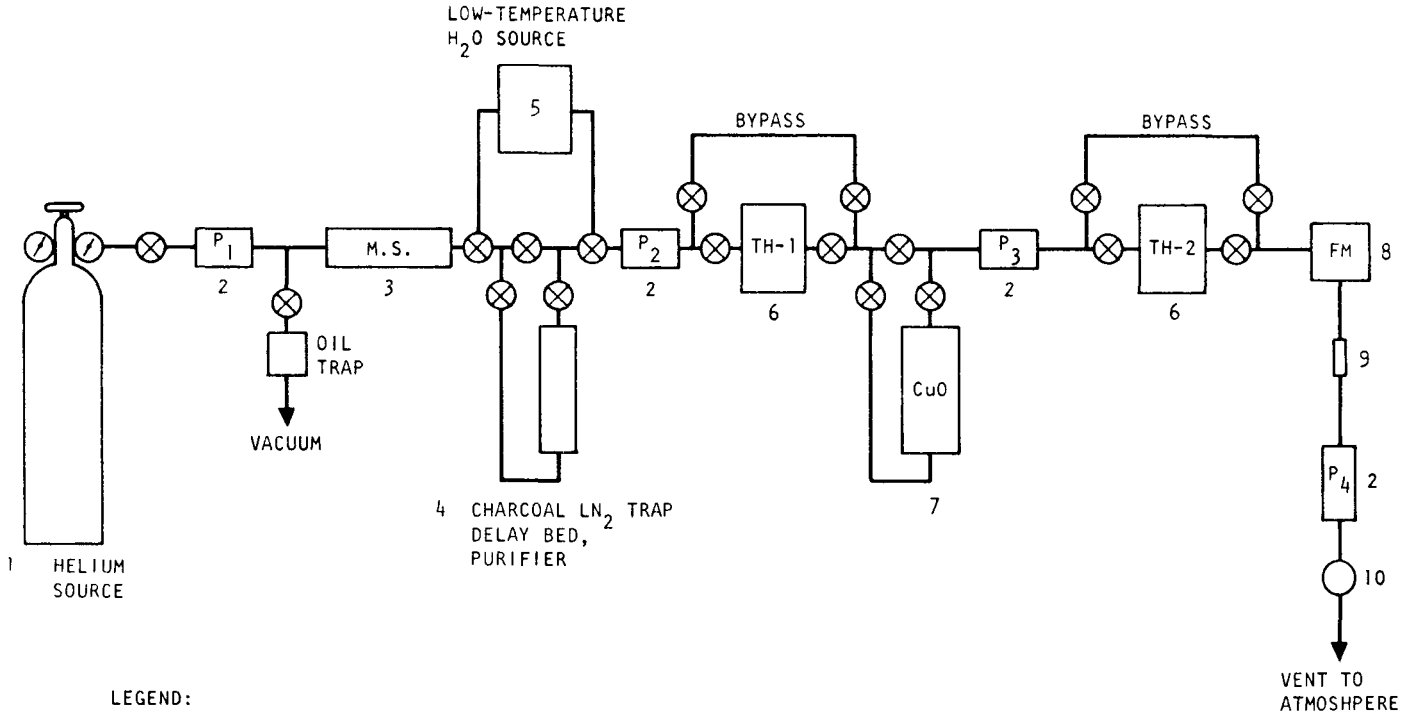

LEGEND:

1 He SOURCE: H_2 (100-, 1000-, AND 10,000-PPM LEVEL IN HIGH-PURITY HELIUM)
2 PANAMETRICS PROBES AT P_1, P_2, P_3, AND P_4
3 MOLECULAR-SIEVE PURIFIER BED
4 CHARCOAL TRAP DELAY BED
5 LOW-TEMPERATURE, ISOTHERMAL H_2O SOURCE
6 THERMOX UNIT FOR OXYGEN MONITOR & H_2/H_2O-LEVEL MONITOR
7 CuO FOR H_2 TO H_2O CONVERSION
8 FLOWMETER (~50 CC/MIN)
9 PRESSURE REDUCER
10 BUBBLER

Fig. 3.12 Schematic of gas-supply apparatus for spacer-rod interaction tests

Some difficulties were also experienced with several moisture probes, which have been returned to the manufacturer. One probe appeared to be attacked by some constituent in the gas stream other than water and another probe failed for no obvious reason. An investigation of the cause of the problem is continuing. Sufficient probes are on hand to continue testing.

Checkout of the apparatus is now in the final stage and initial test data are expected to be obtained during the next quarter.

3.2. BLANKET-ELEMENT ASSEMBLY

The distortion of the highest-powered blanket element rod due to differential thermal and neutron fluence gradients and irradiation-induced creep was analyzed with the CRASIB code. The radial temperature gradients were obtained from a prior conservative thermal analysis and the fluence gradients were the maximum in the blanket region. The total burnup time without rotation or relocation was 5 cycles, or 27,000 hr. The maximum rod displacement was 2 mils, the maximum cladding stress was 3000 psi, and the maximum load on a spacer was 0.7 lb.

3.3. FUEL-ROD MODELING STUDIES

Revision 3 of the LIFE-II code has been put into operation and new predictions are being made for all of the GGA irradiation experiments. Predicted rod expansions for the GB-9 rod are intermediate between predictions with revision 1 and revision 2 of LIFE-II.

The updated code, incidentally, is a convenient source of correlations for swelling and creep of Type 316 stainless steel, both solution-treated and 20% cold-worked.

3.4. LOWER THERMAL SHIELD ASSEMBLY

The preliminary results of the evaluation of the feasibility of upward removal of decay heat from the top surface of molten fuel debris that collects on the lower thermal shield following a postulated core meltdown were reported in the previous quarterly report.[2] That phase of the study considered the case of a fully pressurized reactor primary coolant system and three operating

auxiliary core cooling heat dump loops with auxiliary circulators not operating but with auxiliary-loop isolation valves opened. It was concluded that natural convection circulation above the surface of the molten fuel debris through the auxiliary cooling loops could remove 80% of the total decay heat about 8 to 10 min after shutdown for the least effective flow configuration.

In the extension of that study, the mechanisms involved in the removal of heat from the top surface of the fuel debris utilizing auxiliary coolant-loop components were evaluated for the following conditions:

1. The reference reactor coolant system configuration,
2. An alternative reactor coolant system configuration using series shield cooling,
3. Pressurized or depressurized loop conditions, and
4. Forced or natural circulation of primary coolant gas.

The purpose of this study is to investigate the feasibility of utilizing the auxiliary core-cooling loops to remove upward-directed heat following a postulated core meltdown.

The reference reactor coolant system configuration is shown schematically in Fig. 3.13. If the core melted to the bottom of the reactor cavity, the molten fuel and blanket material would collect in the debris tray in the lower thermal shield, which is shown in Fig. 3.14. The debris tray would be partially cooled by conduction to emergency cooling coils that would be an integral part of the lower thermal shield. A major fraction of the debris heat, however, would be radiated to the shield rods located above the debris tray. For the reference system, it was assumed that the radiated heat is transported to the auxiliary heat exchangers by forced or natural circulation, depending on the pressure level in the system, that the water side of the auxiliary heat exchangers operates at design conditions, and that the auxiliary loop isolation valves are opened to allow the flow of cooling gas through the auxiliary loops. Furthermore, it was assumed that the main loops are isolated and not available to remove heat from the system.

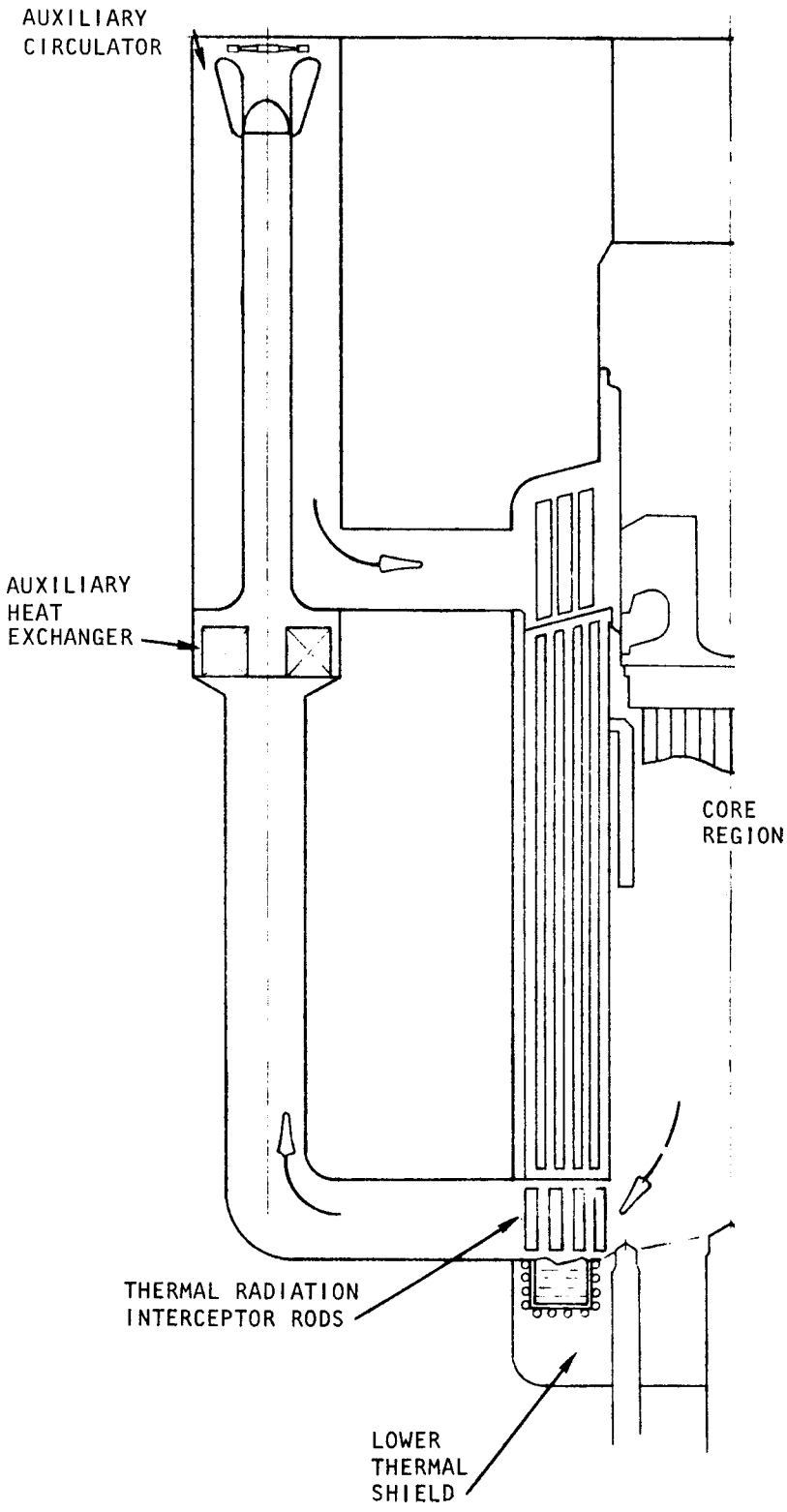

Fig. 3.13 Schematic of reference reactor cooling system configuration

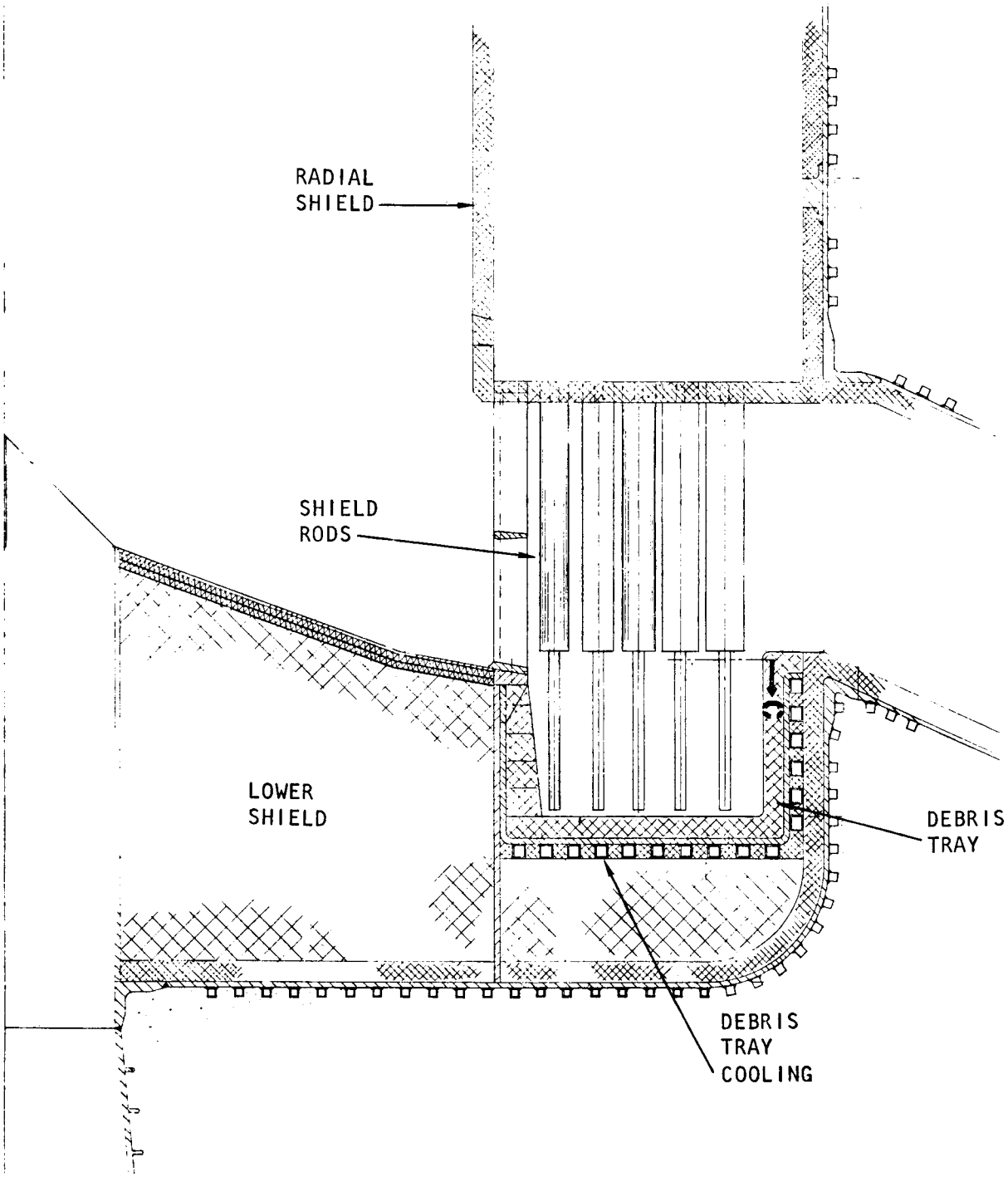

Fig. 3.14 Conceptual design of lower thermal shield assembly and debris tray for reference configuration

An alternative primary coolant system configuration has the coolant flow through the radial shield in series with the core and the auxiliary-loop coolant ducts to the auxiliary heat exchangers are located above the core. This flow configuration results in an increase in the head available for natural circulation for a given driving temperature, compared to the driving head for the reference design.

A schematic of the cooling system for the postaccident fuel containment (PAFC) is depicted in Fig. 3.15. The fuel debris establishes a temperature distribution in the debris tray as the cooling of the material progresses. This results in a multiregion, layered fuel debris structure. Heat is transferred within the debris by conduction in both solid and liquid fuel and by convection in the liquid fuel. Heat is conducted away from the lower surface of the debris. The heat radiated from the upper surface is intercepted by the shield rods that are located in the annular region above the debris.

The shield rods would be cooled by circulation of the coolant, either by forced circulation, which is required for the limiting case of a depressurized system at 2 atm, or by natural convection at higher pressure (85 atm), where the pressure drop for the required flow is of the same order of magnitude as the naturally induced driving pressure.

The coolant flows through the auxiliary loops and deposits heat in the auxiliary heat exchangers, which results in a reduction in coolant temperature. This, in turn, creates a hot leg and a cold leg in the loop, and as a result, there is a density difference in the cooling gas that causes a driving head to be produced. The magnitude of this driving head depends on the helium pressure and on the elevation of the auxiliary heat exchanger over the heat-producing debris.

The heat produced in the core during the first 300 sec following a postulated cessation of coolant flow and a reactor trip is absorbed in the fuel and cladding material and results in the melting and redistribution of the fuel debris. In the process of melting, the volatile fission products are released and are distributed throughout the system. These volatile

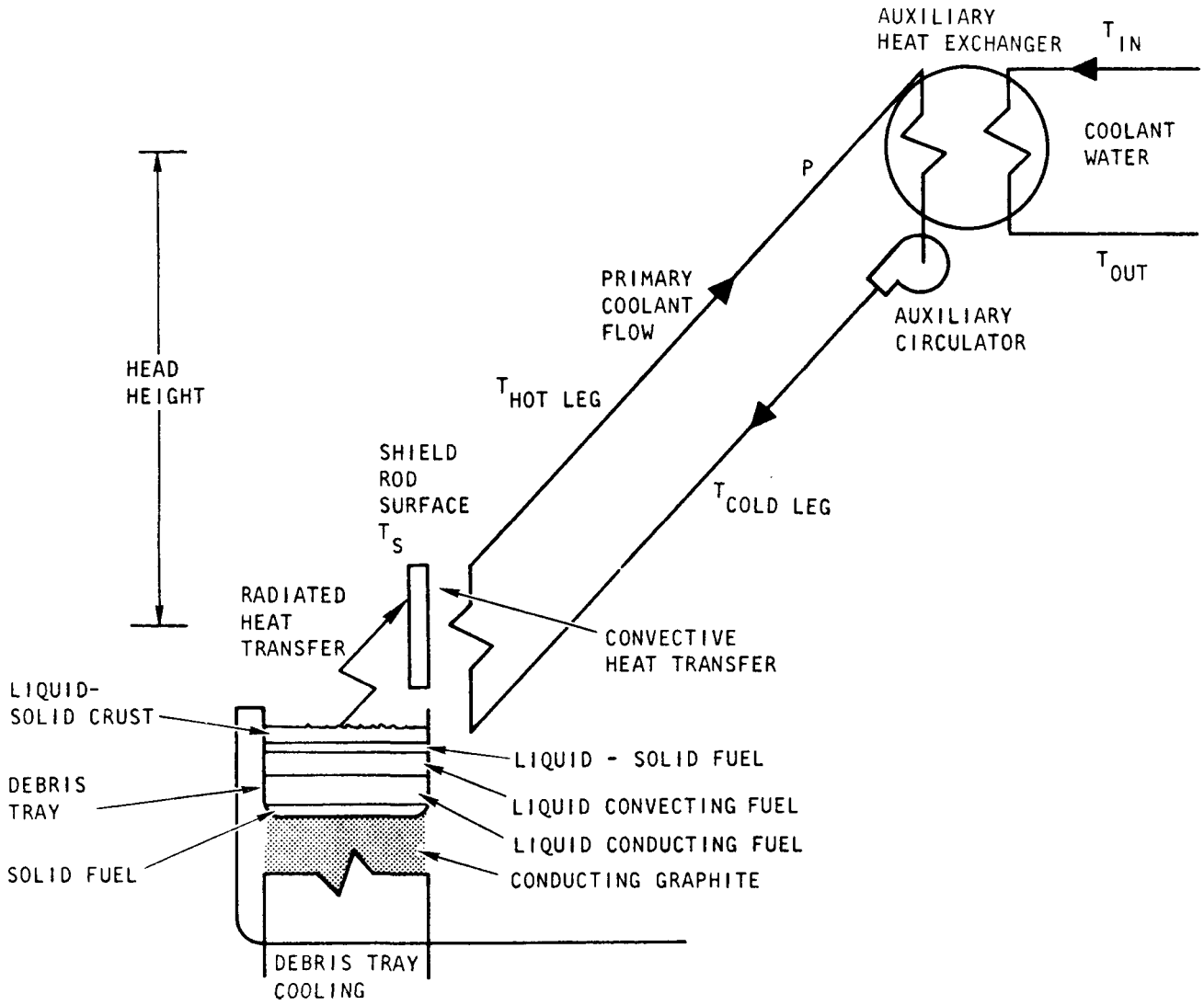

Fig. 3.15 Schematic of convective cooling model for postaccident fuel containment

fission products are estimated to amount to 36% of the total heat generation at that time. The heat generation that remains in the fuel debris at 300 sec would be 19.3 MW. This heat generation rate forms the basis for the results discussed below. The heat generation rate decays substantially during the following few hours. The decay curve is shown in Fig. 3.16. In the first 30 min, the heat generation rate is reduced to 66% of the 300 sec value and in 1.5 hr it is reduced to 50%.

The calculations of the temperature distribution in the debris and the coolant circulation in the loop requires several iterations. For ease of analysis, these problems are calculated separately. The interrelating variable is the temperature of the shield-rod surface and the heat flux. The model for the fuel calculations is:

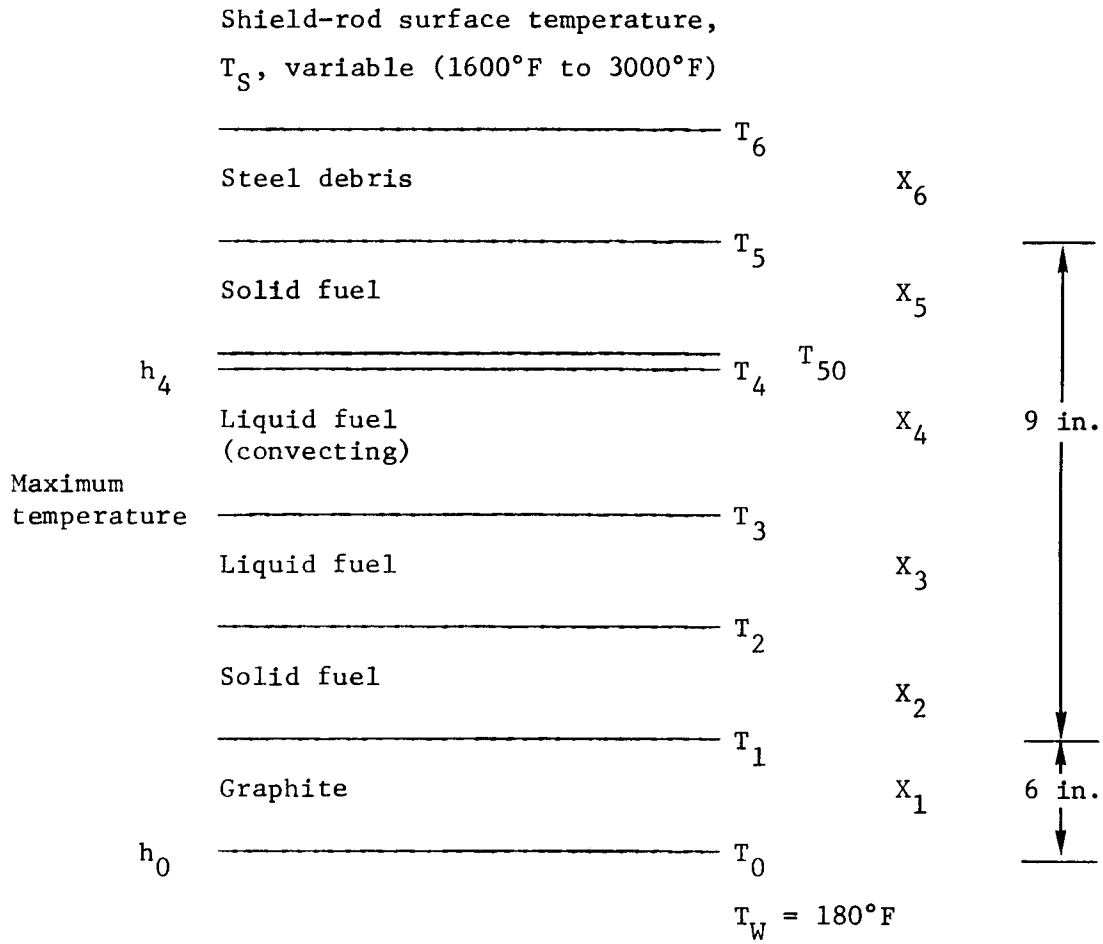

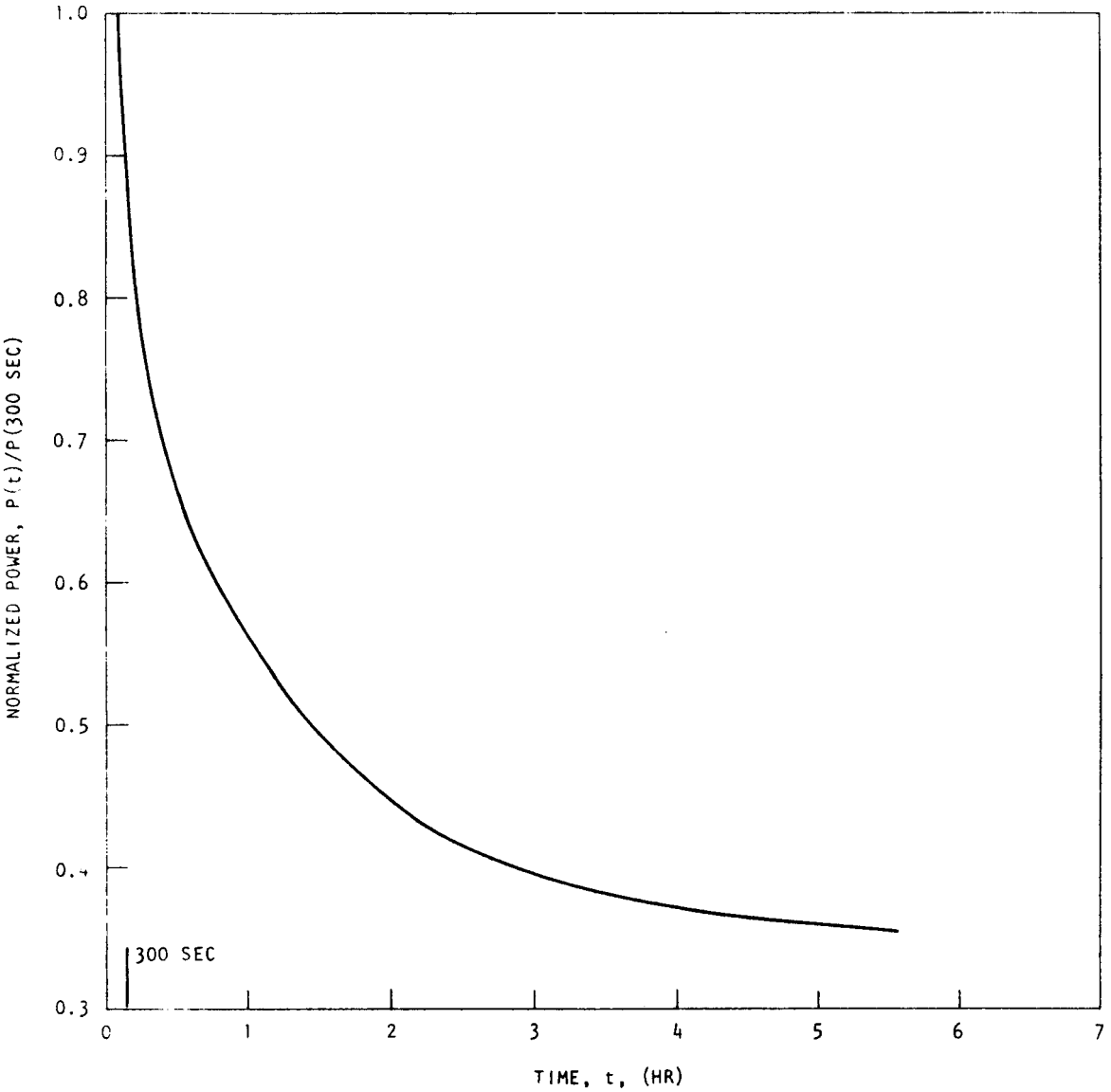

Fig. 3.16 Decay power ratio in debris relative to power at 300 sec

The temperature distribution of the debris is based on a 9-in. slab of fuel (which includes blanket material) on a 6-in. graphite base. Steel debris, ranging in thickness from 3 in. to 0 in., covers the fuel debris. The 3-in. value is based on the total amount of cladding and fuel-element box material. A range of steel thicknesses was considered to account for part of this material remaining on the conical section of the lower thermal shield, which might occur for the larger sections of the fuel-element assemblies that fall onto the cone.

A typical calculation result is given in Table 3.3 for a shield-rod temperature of 2200°F and a 1.5-in.-thick steel debris layer (X_6). The surface temperature of the steel debris is 4880°F and the maximum temperature of the molten fuel (T_3) is 5790°F. No solid fuel crust exists on the upper surface of the fuel. It is assumed that the fuel and steel are layered and immiscible. However, both have internal convection and probably mix, with the result that the steel is vaporized and the thickness of the surface layer diminishes. Figures 3.17 and 3.18 show the thickness of the layers and the temperatures of the interlayers for a 3-in.-thick surface debris of steel as a function of the shield-rod surface temperatures.

Table 3.3

TYPICAL TEMPERATURES AND MATERIAL THICKNESSES IN MOLTEN DEBRIS

Temperatures (°F)		Thicknesses (in.)	
T_S	2200	X_6	1.50
T_6	4880	X_5	0.00
T_5	5115	X_4	7.12
T_{50}	5115	X_3	1.04
T_4	5115	X_2	0.84
T_3	5790	X_1	6.00
T_2	5982		
T_1	995	Heat-transfer Coefficients (Btu/(hr)(ft^2)(°F)	
T_0	278	h_4	4400
T_W	180	h_0	880

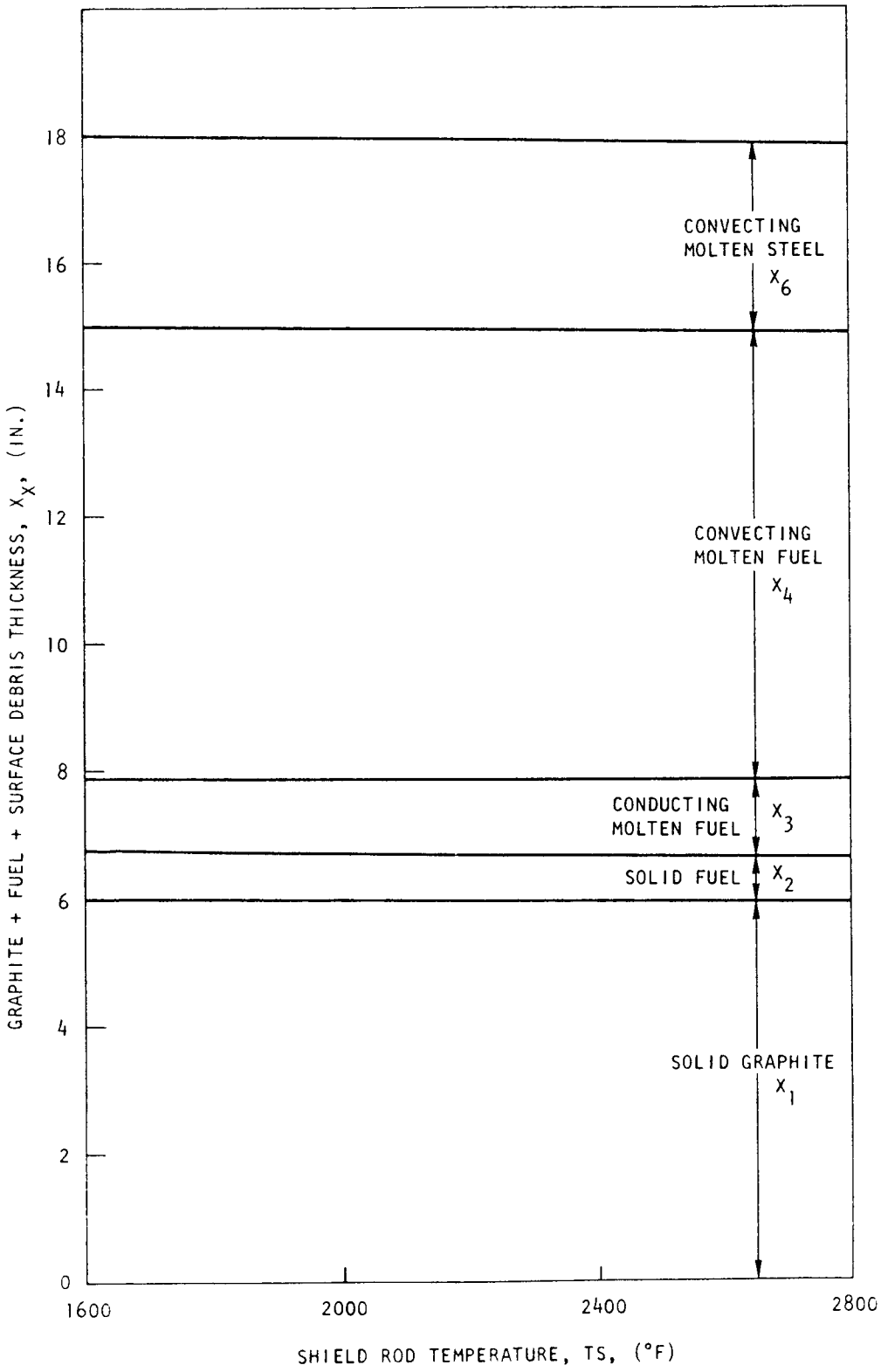

Fig. 3.17 Debris thickness vs. shield-rod temperature for 3-in. steel surface debris

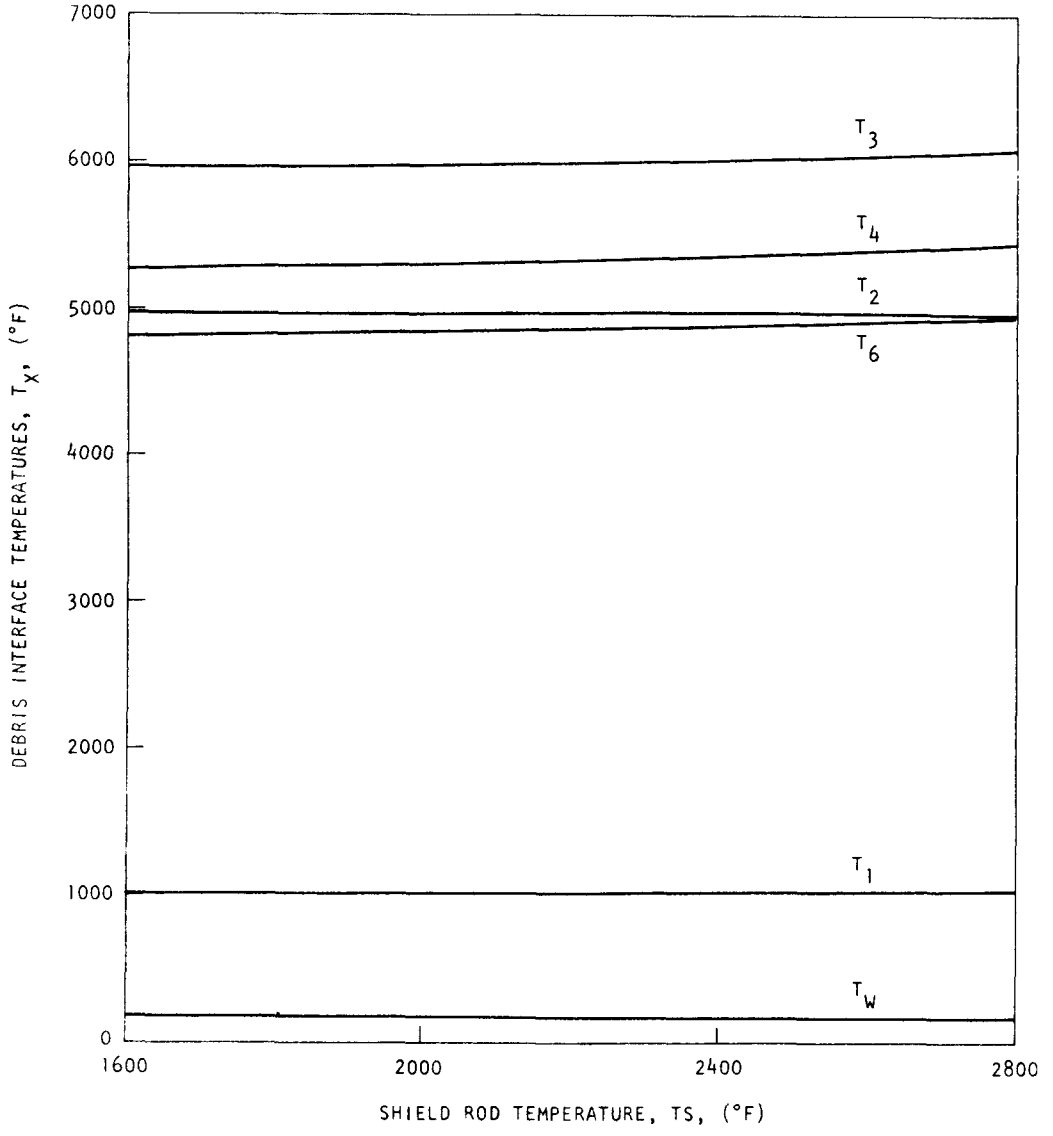

Fig. 3.18 Debris interface temperatures vs. shield-rod temperature for 6 in. of graphite and 3 in. of surface material

In general, the results for interlayer temperatures and thicknesses are almost independent of the shield-rod temperatures. This is expected since the heat rejection goes as the absolute temperature to the fourth power. The heat rejection to 3000°F, which is equivalent to 4830°F rejecting to 1600°F, would increase the rejecting temperature to 5030°F or only 200°F change in rejecting temperature for a 1400°F change in sink temperature. The resulting heat rejection is 79% in the upward direction and 21% in the downward direction. The Rayleigh number is about 0.4×10^{10}, which indicates a highly turbulent flow in the convective layer. The resulting Nusselt number is about 120, indicating an effective increase 120 times the normal material conductivity. The minimum velocity in the convective material is low, however, at 0.06 in./sec. Actual velocities are probably a factor of 10 larger.

The maximum temperature of the molten fuel (T_3) is relatively high for all cases and is always greater than the boiling point of steel. It depends on the thickness of the upper solid-liquid fuel layer, which is very thin in all cases and probably does not form until a substantial power reduction occurs. Any fuel vaporization that occurs will tend to break up the thin layer of solid fuel. For these conditions, fuel vaporization could occur for the case of a 3-in.-thick layer of steel. This vaporized fuel should condense as it passes through the subcooled layer of fuel and steel, which would tend to enhance the heat transport through the debris without any substantial loss of fuel material to the convecting gas system.

The results for the reference system in which 10 of the 28 rows of shield rods are cooled by each duct are shown in Fig. 3.19. Heat rates are shown for each loop. The heat rejection curves are plotted as a function of pressure. Calculations were carried out down to 5 atm. The code used could not be made to converge at a lower pressure. The curves are very steep at the low pressure and may be asymptotic to a pressure between 2 and 5 atm, which would explain the lack of convergence. The significance of this is the difficulty in estimating the time beyond which forced circulation would not be required for a depressurized system.

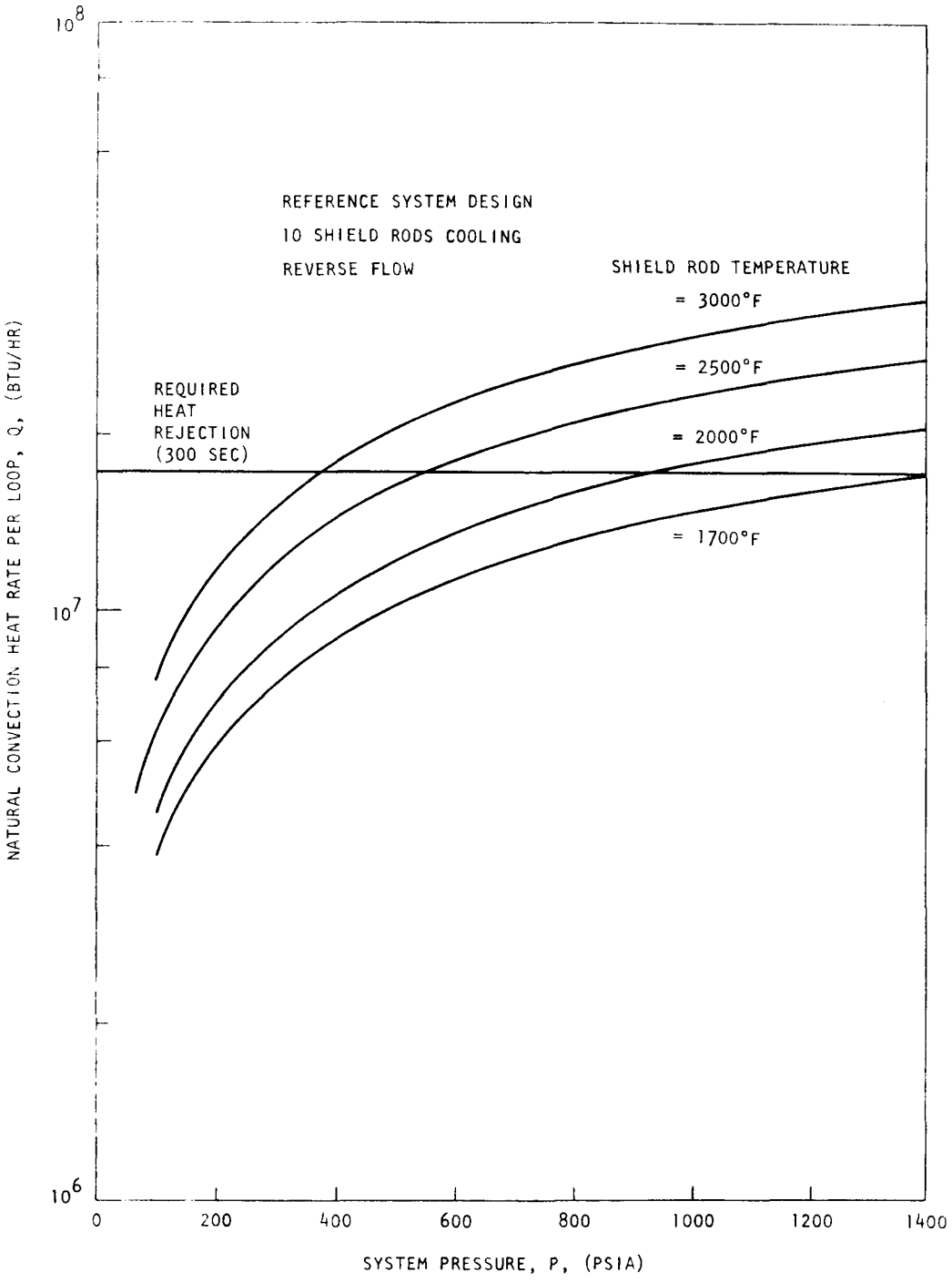

Fig. 3.19 Natural convective heat rate vs. system pressure

The required heat rejection for each loop is shown; the intersection of this curve with the convection curves for various shield-rod surface temperatures indicates the lowest system pressure required to sustain natural convective cooling of the debris. The cooling can be improved if the area of the shield-rod surface cooled by natural convection can be increased. This could be accomplished by making the lower auxiliary duct oval in shape and by including flow directors. For the case of 15 rows of shield rods cooled by widened ducts, the heat-transfer area is increased by 50% and so is the heat rejection capacity. For the case of a shield-rod surface temperature of 2500°F, the minimum pressure for natural circulation drops from 540 to 420 psia.

For a series-cooled shield, a similar set of curves shows slightly reduced performance over the 10-row shield cooling but results in a uniform cooling of the debris that the reference design cannot achieve because of the flow direction characteristics of the ducts. After some period of time, two-loop operation will also be permissible for the series cooled shield concept.

Natural circulation could provide adequate heat removal at a pressure less than operating pressure but not in the depressurized (2 atm) condition. It is most probable that either of the two extreme system pressures would exist and not some intermediate pressure. For the case of full system pressure, Fig. 3.20 shows the heat rejection capability of the loops for various shield-rod surface temperatures. The heat rejection requirement is also shown. The shield-rod surface temperatures for the required heat rejection are 1750°F and 1600°F for the reference design with 10-row and 15-row shield-rod cooling and 2200°F for the alternative design with series shield cooling. If 2500°F is considered an upper limit of shield-rod surface temperature in order to prevent cladding melting, then, for the case of the series shield, two-loop operation can occur after 7 min.

Forced circulation could provide adequate heat removal for all cases including the depressurized case. Figure 3.21 shows heat rejection curves for 10-row and 15-row shield-rod cooling as a function of shield-rod

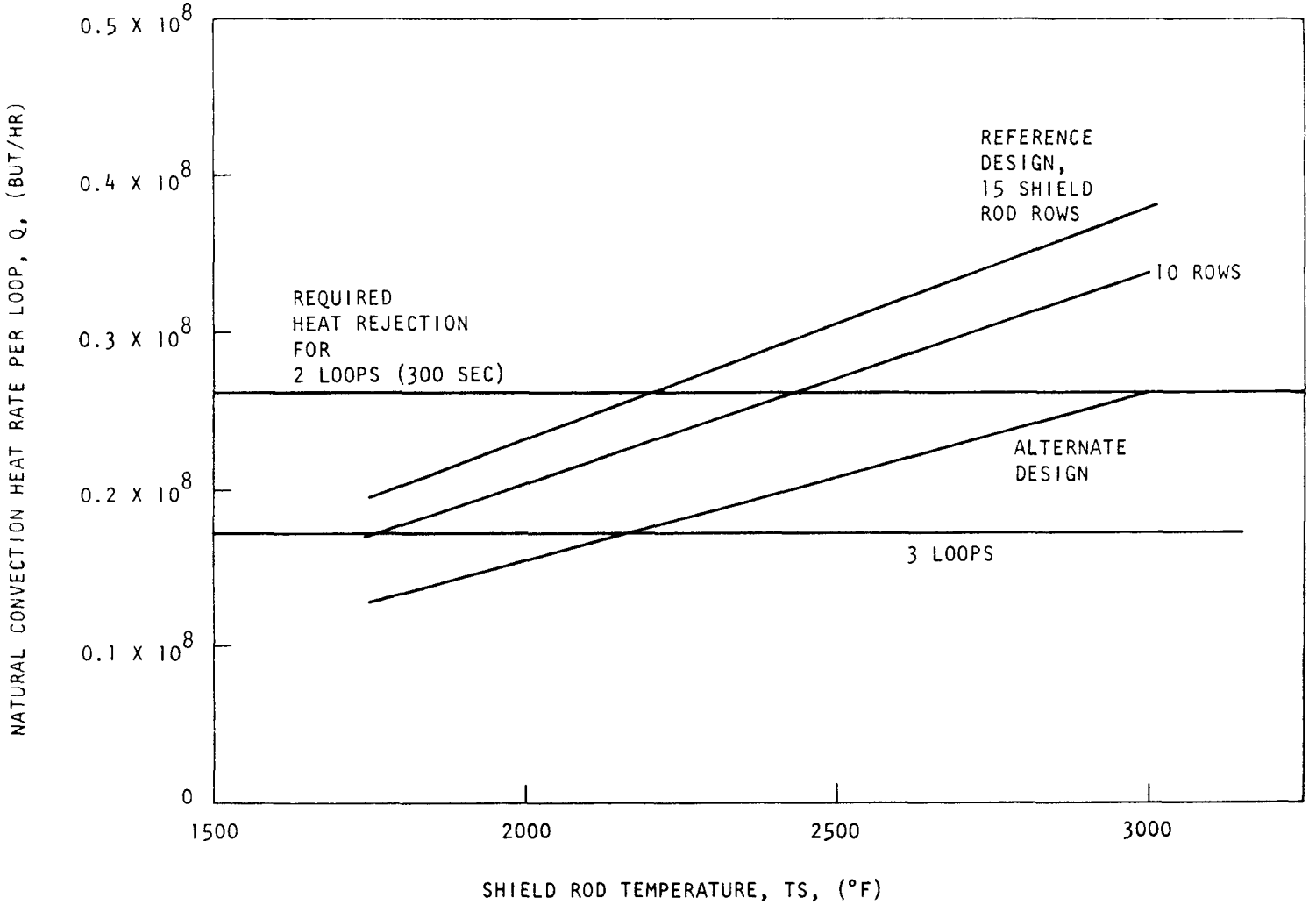

Fig. 3.20 Natural convection capability (pressure = 1250 psia)

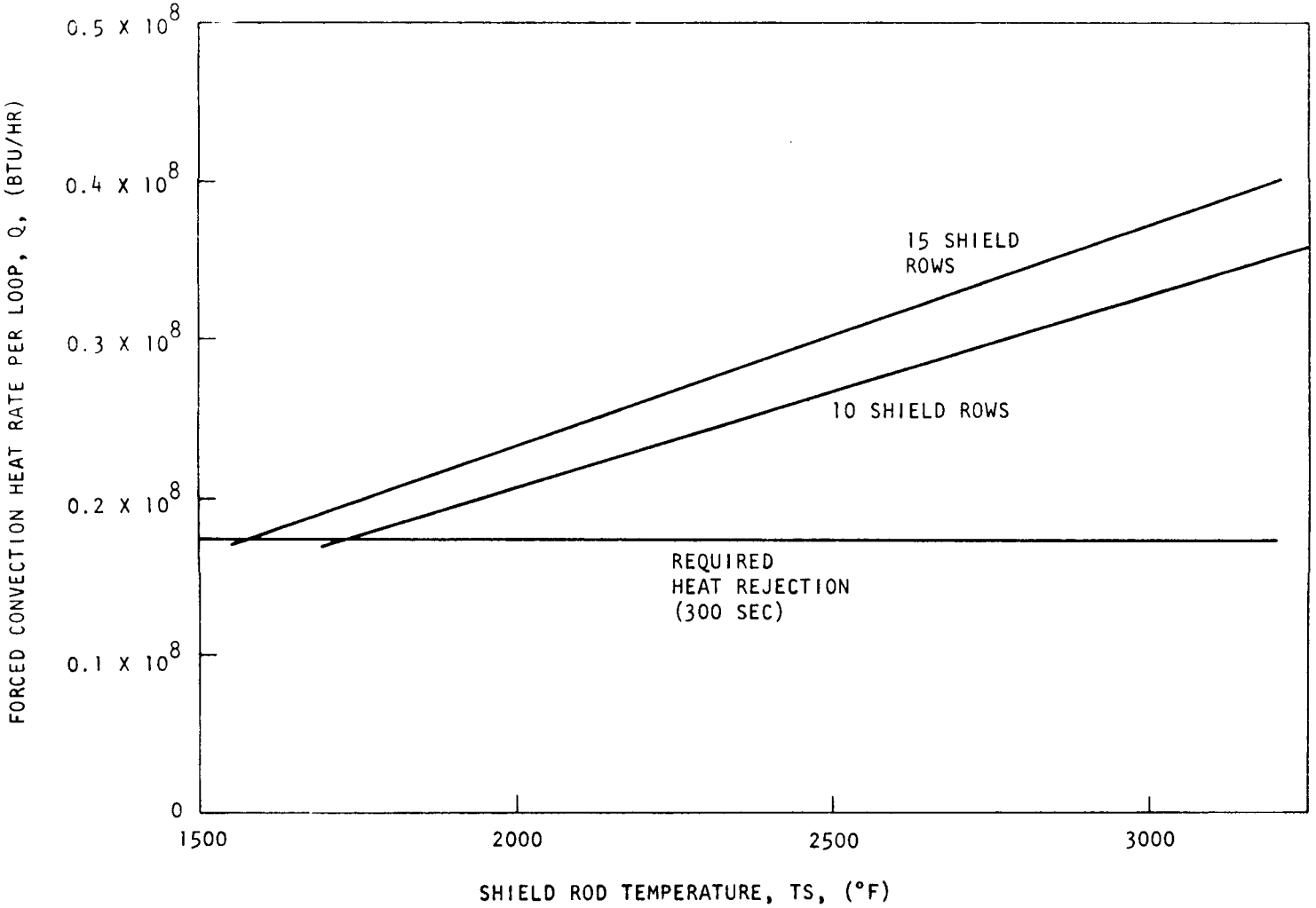

Fig. 3.21 Forced circulation with reference system design (for pressure at 30 psia)

temperature. The required heat rejection occurs at a shield-rod surface temperature of 1750°F and 1600°F. For the series cooled shield, the required heat rejection occurs at a shield surface temperature of 2250°F. For a 2500°F limit, two loops are able to meet the cooling requirements after about 9 min. A single forced-circulation loop would be adequate after 3.5 hr.

The flow achieved by natural circulation with 1250 psi pressure is relatively high—54,600 lb/hr per loop for a shield-rod surface temperature, T_S, of 2000°F. The Reynolds numbers at the shield rods and in the auxiliary heat exchanger are 42,290 and 5,370, respectively. The heat-transfer coefficient for the gas side at each location is 71 and 117 Btu/(hr)(ft^2)(°F) and the overall heat-transfer coefficient for the auxiliary heat exchanger is 107 Btu/(hr)(ft^2)(°F). The water-temperature rise is 122°F, and the temperatures for the hot leg and cold leg are 638°F and 336°F, respectively.

The series cooled shield configuration with natural circulation has a higher driving pressure and flow. The convected heat is reduced by 25% because of the reduced mass flux that results from a higher flow area at the shield rods. Adjustment of the shield-rod design could result in improved performance. A geometric optimization can be performed on the selected PAFC cooling system.

Typical results for forced circulation for a pressure of 2 atm indicate a flow of 57,420 lb/hr per loop and a pressure drop of 1.3 psia. Temperatures are about the same as for the natural circulation case for the reference system, which indicates a balanced design condition for two relatively different cooling configurations.

In drawing conclusions from a study of this type, consideration must be given (1) to the very large uncertainties associated with the physical mechanisms involved in heat removal from the PAFC, (2) to the unknown properties of materials at the abnormally high temperatures involved, and (3) to the actual distribution of the heat produced in the system, particularly from the volatile fission products. Within these limitations, the following tentative conclusions have been drawn from this study:

1. Forced circulation through the auxiliary loops may be a feasible way to provide adequate heat removal from the debris with a depressurized or pressurized system if all three auxiliary loops operate with nominal conditions for 30 min and two loops are operational for the series cooled shield configuration after 30 min.

2. Natural circulation through the auxiliary loops could only provide adequate heat removal from the fuel debris tray if

   (a) System pressure is maintained above 600 to 900 psi,

   (b) Means are provided for opening the auxiliary loop valves,

   (c) Cooling water is provided to the auxiliary heat exchangers, and

   (d) The design of the auxiliary-loop ducts is modified to provide better flow distribution.

3. The series cooled shield configuration would offer a significant advantage over the reference coolant system configuration for uniform heat removal from the debris regardless of the number of operating loops.

4. Temperatures of surfaces heated by thermal radiation from the fuel debris would not exceed 2500°F (the melting temperature of steel) for the cooling cases considered and would be below 2000°F in 30 min.

5. Internal convection within the molten fuel debris would be the principal heat-transport mechanism in the upward direction and has the effect of a magnification of about 120 in the thermal conductivity of the molten fuel. The boiling temperature of the fuel would not be exceeded for the cases studied.

REFERENCES

1. "Gas-Cooled Fast Breeder Reactor Quarterly Progress Report for the Period August 1, 1972, through October 31, 1972," USAEC, Report GA-A12421, Gulf General Atomic, December 8, 1972.

2. "Gas-Cooled Fast Breeder Reactor Quarterly Progress Report for the Period November 1, 1972 through January 31, 1973," USAEC, Report GA-A12530, Gulf General Atomic, March 8, 1973.

3. Sutherland, W. H., and V. B. Wotwood, Jr., "Creep Analysis of Statically Indeterminate Beams—CRASIB, Users Guide and Program Manual," USAEC, Report BNWL-1362, Battelle Northwest Laboratories, June 1970.

4. Pellaud, Bruno, "The Physics Design of the Gas-Cooled Fast Breeder Reactor Demonstration Plant," USAEC, Report GA-10509, Gulf General Atomic, August 29, 1971.

5. Boltax, A., et al., "Oxide Fuel Element Development Quarterly Progress Report for the Period Ending June 30, 1972," USAEC, Report WARD-3045T3-7, Westinghouse Electric Corporation, September 1972.

6. Boltax, A., et al., "Oxide Fuel Element Development Quarterly Progress Report for the Period Ending September 30, 1972," USAEC, Report WARD-3045T3-9, Westinghouse Electric Corporation, January 1973.

7. Roark, R. J., Formulas for Stress and Strain, 4th ed., McGraw-Hill Book Company, 1965.

4. TASK 4160—PRESSURE EQUALIZATION SYSTEM FOR FUEL

Near the end of the last quarterly period, the planning document for the fuel pressure equalization system was submitted to the Division of Reactor Development and Technology (DRDT) for review. During this reporting period, the supplementary information requested by DRDT on the pressure equalization system was prepared and submitted. In addition, a presentation was made to the DRDT staff on the pressure equalization system development program, the design criteria and systems description documents, and plans for implementing and conducting the FY 73 portion of the program. Other work on this task was spent on devising various alternative plans for implementing the program, contingent upon the authorization date and the end of the fiscal year.

5. TASK 4200/4400—FUELS AND MATERIALS DEVELOPMENT

5.1. THERMAL-FLUX IRRADIATION EXPERIMENTS

5.1.1. Irradiation Capsule GB-9

As no further postirradiation examination will be done at Argonne National Laboratory (ANL) East of the vented fuel rod capsule GB-9, sections of the GB-9 sweep line, the activated charcoal trap, and a section of the cladding for determination of the temperature by Kr^{85} release will be shipped to GGA and samples of the GB-9 fuel will be sent to ANL West for burnup analysis.

5.1.2. Irradiation Capsule GB-10

The GB-10 vented-fuel-rod sweep-gas capsule experiment has reached a burnup of ~20,000 MWd/Te in the ORR while operating at a linear heat-generation rate of 12 kW/ft and a maximum cladding temperature of 565°C. The capsule is being operated at 12 kW/ft until steady fission-gas release conditions are attained. After this initial period, the heat-generation rate will be increased to 13.5 kW/ft until steady fission-gas release rates are again attained, and then it will be increased to 14.8 kW/ft. The capsule will continue to be operated at 14.8 kW/ft for the remainder of irradiation to a burnup goal of 75,000 MWd/Te.

During this reporting period, several analyses were made of the data taken from capsule GB-10. These included a comparison of the calculated and measured release of radioactive fission gases from the solid-state oxide fuel matrix and analyses of the relative transport delay times in the various parts of the GB-10 fuel rod, the release of activity on initial startup, and leaking-rod simulation tests.

5.1.2.1. Measured Release of Active Fission Gas from Solid-phase Fuel. The active fission-gas release from the GB-10 fuel rod was measured directly by flowing sweep gas through the fuel region (i.e., in through the bottom of the fuel and out through the bottom of the blanket) during operation at

12 kW/ft. Samples of the sweep gas were then analyzed by gamma spectrometry. The results of one set of measurements taken at ~6,800 MWd/Te are given in Table 5.1. These are compared with the computed release values at the three linear heat-generation rates and at different burnups. The calculations were made with the LIFE-II code using the diffusion release model and the diffusion coefficients derived by Findlay.[1] Also, in the calculations it was necessary to take into account the self-shielding effect on the radial power distribution of the rod not only to determine the distribution of fission products generated but also the radial temperature distribution. The measured releases at 6,800 MWd/Te are much lower than the calculated values, at least at the 12 kW/ft power level. Additional measurements were taken at a burnup of 17,000 MWd/Te at 12 kW/ft but the data have not yet been processed. Similar measurements are planned to be made at the two higher operating levels.

5.1.2.2. Measured Gas-phase Fission-product Transport. The diffusion transport of fission products in the gaseous and solid phase were readily separable in capsule GB-10. Transport through the upper blanket region of the rod is measured directly. This is done by taking samples during two sweep-gas flow modes—in through the top of the trap and out through the bottom of the trap (TT-BT) to measure the fission products emerging from the top of the upper blanket and in through the top of the trap and out through the bottom of the blanket (TT-BB) to measure the fission products entering the bottom of the upper blanket. The effective transport delay time in the blanket region can be expressed by the following relation:

$$t_i = \frac{T_i^{1/2}}{0.693} \ln\left[\frac{EF\ (\text{bottom of blanket})}{EF\ (\text{top of blanket})}\right] ,$$

where t = effective transport delay time through the region of interest,

$T_i^{1/2}$ = half-life of the ith isotope,

EF = escape fraction.

One set of measurements of transport delay time of gaseous fission products in the upper blanket region of the GB-10 rod was made at ~6,800 MWd/Te. These are compared with calculated values in Table 5.2. Considering the

Table 5.1

MEASURED AND CALCULATED RELEASE FRACTIONS IN CAPSULE GB-10

(Release fractions in %)

Isotope	Half-life	Measured, 12.0 kW/ft, 6,800 MWd/Te	Calculated			
			12.0 kW/ft, 7,667 MWd/Te	12.0 kW/ft, 15,300 MWd/Te	13.5 kW/ft, 25,000 MWd/Te	14.8 kW/ft, 40,250 MWd/Te
Xe-133	5.27d	5.20	25.2	22.8	34.1	44.3
Xe-135	5.76h[a]	1.04	8.55	7.50	12.8	18.7
Xe-135m	15.3m	0.52	1.52	1.33	2.34	3.56
Xe-138	17.0m	0.28	1.61	1.40	2.47	3.75
Kr-85m	4.40h	1.01	7.73	6.88	11.1	15.6
Kr-88	2.80h	0.38	6.25	5.55	8.98	12.8
Kr-87	1.30h	0.34	4.32	3.83	6.25	8.96

[a]Effective half-life in the ORR thermal flux.

complexities of the diffusion processes that occur in a fuel rod, the agreement between calculated and measured values is believed to be good.

Table 5.2

MEASURED GASEOUS FISSION-PRODUCT RELEASE FROM GB-10 OXIDE FUEL AND COMPARISON OF MEASURED AND CALCULATED UPPER BLANKET TRANSPORT TIME

Isotope	Half-life	Release Fraction in Fuel (%)	Effective Release Delay Time in Fuel	Upper Blanket Transport Time	
				Measured	Calculated
Xe-133	5.27d	5.20	22.5d	1.76d	0.23d
Xe-135	5.76h[a]	1.04	38.0h	5.84h	4.70h
Kr-85m	4.40h	1.01	29.2h	2.15h	3.94h
Xe-135m	15.3m	0.52	116m	42.2m	100m
Kr-88	2.8h	0.38	22.5h	1.38h	3.55h
Kr-87	1.3h	0.34	10.7h	1.72h	2.80h
Xe-138	17.0m	0.28	144m	32.0m	98m

[a]Effective half-life in ORR thermal flux.

5.1.2.3. Initial Startup Activity. The activity passing through the sample-line monitor during initial startup of capsule GB-10 is shown in Fig. 5.1. The power level of the capsule is indicated by the temperature of the cladding, which is monitored by thermocouples imbedded in the inner surface of the Zircaloy sleeve, that surrounds the fuel rod and serves as a thermal barrier in the capsule. Also shown are the corresponding linear heat-generation rates. The sweep-gas flow mode was in through the bottom of the fuel and out through the top of the trap (BF-TT), i.e., through the entire rod. New saturation levels of activity were reached following each step increase in power in less than 1 hr. It is presumed that this is short-lived activity released primarily from the central zone of the fuel rod and fission fragment recoil from the fuel surfaces.

The activity released by the fuel remained low until the linear heating rate exceeded about 10.5 kW/ft and the cladding maximum outer surface temperature exceeded about 500°C (a thermocouple reading of ~420°C). When the power level was raised to 12 kW/ft and held at that level, the

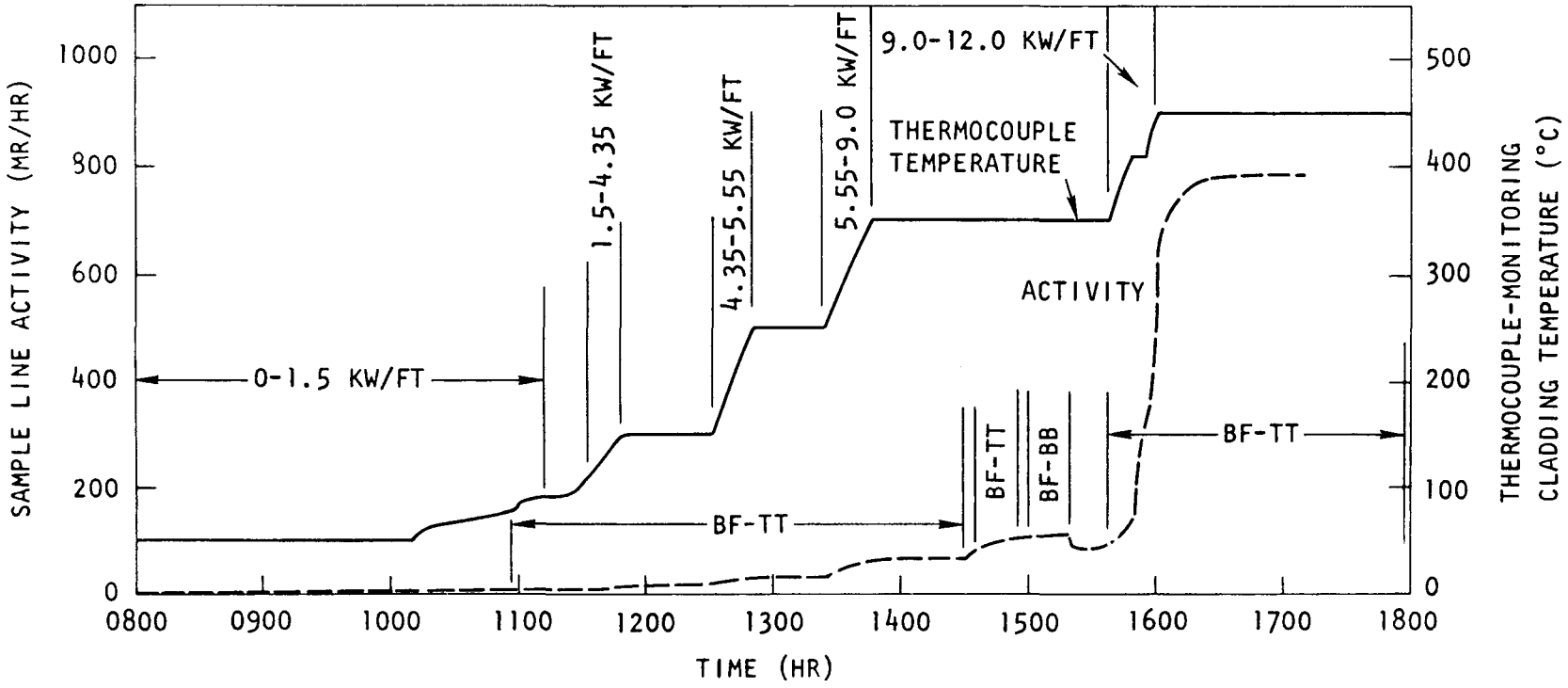

Fig. 5.1 Initial startup conditions of capsule GB-10

activity rose very rapidly, by a factor of ~6.5, whereas the outer surface temperature of the cladding increased 100°C. The factor of 6.5 increase in activity per 100°C is less than the factor of 10 increase per 100°C found in capsule GB-9 at 14.8 kW/ft and a 685°C cladding temperature.

It should be noted that although bursts of fission gas from the fuel rod during startup and shutdown have been reported by other investigators,[2] there were no indications of bursts of activity from fission-gas release from the solid-pellet fuel in capsule GB-10 or the annular-pellet fuel in capsule GB-9 during startup or shutdown. When no bursts were observed in GB-9, it was believed that perhaps the test arrangement might have smeared out the activity pulse and thus masked such an event. In capsule GB-10, however, it has been possible to sweep carrier gas over the fuel so that a direct measurement could be made of any sudden release of activity, but none was observed.

5.1.2.4. Applicability of Capsule GB-10 Results to the GCFR. The fission-gas release and transport measured in capsule GB-10 are compared with those calculated for the GCFR reference design in Table 5.3. The information in Table 5.3 summarizes the relative importance of the solid-phase and gas-phase diffusion processes in the control of radioactivity from vented (pressure-equalized) GCFR fuel rods. The major difference between the capsule test conditions and reactor conditions is the percentage of the total delay time associated with the solid-phase and gas-phase diffusion processes. Comparison of the gas-phase transport delay times through the three regions of the rod show the relative importance of these regions in delaying the transport of fission gases. It is apparent from the measurements that the delay during solid-phase diffusion between fission and release to the gas phase is the most important and the limiting process. However, in the GCFR reference design fuel element where the upper blanket is ~17 in., compared to ~2 in. in the capsules, the limiting process is gas-phase diffusion, with the upper blanket being the most effective region in delaying fission-product transport. It is expected that a greater percentage of the total delay time will be in the gas phase when the power and temperature level of the fuel rod in GB-10 is raised to the higher operating levels. Some idea of the change to be

Table 5.3

COMPARISON OF ACTIVE FISSION GAS TRANSPORT DELAY TIMES OF CAPSULE GB-10 AND GCFR REFERENCE DESIGN

Isotope	Half-life	Solid-phase Transport Delay Times (% of total time)	Gas-phase Transport Delay Times (% of total time)			Total Solid- and Gas-phase Transport Delay Times
			Fuel	Blanket	Trap	
Vented Capsule,[a] 12.0 kW/ft at 565°C Maximum Cladding Outside Temperature						
Kr-85m	4.4h	81.3	3.96	5.99	8.72	35.9h
Kr-87	1.3h	71.8	6.91	11.5	9.79	14.9h
Kr-88	2.8h	81.8	3.39	5.01	9.85	27.5h
Xe-133	5.27d	83.4	3.44	6.52	6.63	27.0d
Xe-135m	15.3m	49.4	7.92	18.0	24.7	235m
Xe-135	5.76h[b]	68.2	3.59	10.5	17.8	55.7h
Xe-138	17.0m	54.8	11.1	12.2	21.9	293m
GCFR Reference Design,[c] 15.0 kW/ft at 700°C Maximum Cladding Outside Temperature						
Kr-85m	4.4h	14.3	17.2	58.9	9.67	111h
Kr-87	1.3h	10.1	11.2	67.7	11.0	56.9h
Kr-88	2.8h	12.7	14.8	62.3	10.2	85.8h
Xe-133	5.27d	26.2	35.9	32.8	5.14	39.3d
Xe-135m	15.3m	6.10	5.68	74.9	13.3	1476m
Xe-135	9.13h[d]	18.0	19.8	53.4	8.73	152h
Xe-138	17.0m	2.70	2.54	89.1	5.64	3653m

[a]Measured release and delay times in fuel, blanket, and trap of capsule GB-10.

[b]$T_{1/2}$ (effective) = 5.76 h in thermal flux.

[c]Calculated values, based on Findlay's release model and gaseous diffusion transport.

[d]$T_{1/2}$ = 9.13h in fast flux.

expected at the higher power levels is shown in Table 5.3 for the calculated transport delay times for gaseous fission products through the solid phase for the GCFR reference design.

5.1.2.5. Simulation of Leaking Rod. One of the unique features of capsule GB-10 is the capability to simulate a cladding leak in a GCFR fuel rod. In the GCFR, the internal pressure of the fuel rods is lower than the external coolant pressure, so inleakage results if a cladding defect develops. The inleaking coolant gas sweeps the gaseous and volatile fission products through the rod; the volatile fission products remain in the rod or the rod trap and the gases are carried into the monitor lines. A change in the transport time from gaseous diffusion conditions to the leakage convective flow conditions results in a greater activity level at the monitor, which indicates the advent of a leak and provides at least a crude measure of the leak rate.

Leak simulation tests have been conducted in capsule GB-10 at 250, 7,620, 8,700, 9,550, 13,000, and 15,500 MWd/Te burnup. It is planned to continue such tests at various burnups during the remainder of the experiment. The amplification of the activity at the sample-line monitor at the onset of a simulated rod leak of ~1100 cm^3(STP)/min with a transport time of ~43 sec from the fuel to the monitor has been found to vary from a factor of ~80 to a factor of 100. The amplification factor depends on the transport time from the fuel to the monitor when there is no leak and when there is a "leaking" rod. The transport time under leaking conditions depends on the leak rate. Thus, once the "no-leak" basis has been established, the size of a leak can be determined by the linear function of transport time since the activity released is a mixture of isotopes whose distribution changes with the transport time. The change in the vented fraction measured in capsule GB-10 for a number of isotopes is shown in Table 5.4. Preliminary calculations indicate maximum aplifications are to be expected in GCFR plants. A computer code is being developed to model the processes by which the activity changes at the monitors if a leak should occur. Data produced by the simulation of a leaking fuel rod in capsule GB-10 will be used to evaluate the correctness of the computer code model.

Table 5.4

CHANGE IN VENTED FRACTION WITH ONSET OF A 1150 CM^3 STP/MIN SIMULATED LEAK

(6,800 MWd/Te burnup)

Isotope	Half-life	Vented Fraction		Vented Fraction Ratio (Leak/No Leak)
		BF-TT (leak)	TT-TT (No Leak)	
Xe-133	5.27d	0.11	0.058	1.90
Xe-133m	2.30d	0.085	0.045	1.89
Xe-135	5.76h[a]	0.050	0.007	7.14
Xe-138	17.0m	0.016	2.7×10^{-5}	593
Xe-135m	15.3m	0.0115	3.3×10^{-5}	348
Xe-139	41.0s	6.0×10^{-3}	nd[b]	nd
Xe-137	3.90m	3.9×10^{-3}	nd	nd
Kr-85m	4.40h	0.036	0.016	2.25
Kr-88	2.80h	0.025	0.00075	3.33
Kr-87	1.30h	0.022	0.0029	7.59
Kr-89	3.20m	0.0032	nd	nd

[a]Effective half-life in ORR thermal flux.

[b]Not detected.

5.2. FAST-FLUX IRRADIATION EXPERIMENTS

5.2.1. Fast-flux Irradiation Experiment F-1 (X094A)

The seven encapsulated fuel rods in the F-1 (X094A) experiment are currently being subjected to a second interim examination, which is being made after burnup exposures up to 56,000 MWd/Te were reached in the initial six fuel rods. (Capsule G-3 was replaced with capsule G-8 during the first interim examination.) Neutron radiographs of the seven capsules have not yet been made. The current burnup exposures and operating conditions for the fuel rods are given below.

Capsule	Burnup (MWd/Te)	Linear Heat-generation Rate (kW/ft)	Calculated Cladding Outside Temperature (°C)
G-1	56,000	16.1	783
G-2	54,600	15.5	753
G-8	27,000	13.7	702
G-4	51,800	13.3	708
G-5	52,800	14.3	669
G-6	50,000	14.4	721
G-7	49,000	13.8	612

Capsules G-1, G-2, G-5, G-6, and G-7 will be removed and replaced during the current interim examination. When these fuel-rod capsules have been replaced with unirradiated fuel-rod capsules and the subassembly reconstituted, irradiation of the experiment will continue to a burnup goal of 100,000 MWd/Te in the remaining initial fuel-rod capsule (G-4).

All seven fuel rods were leak-checked by gamma counting for Xe^{133} in the capsule plenums. No xenon was detected in any of the capsule plenums, which indicated that all of the rods were intact. These results were substantiated by confirming the presence of Xe^{133} in the rod plenums of five of the rods.

Precision gamma scans were made in selected regions of the fuel rod in capsule G-1 (containing the highest temperature rod—a cladding outside temperature of 783°C) and of the rods in capsules G-4 and G-8 as shown in Table 5.5.

Table 5.5

PRECISION GAMMA SCANS OF FUEL RODS IN CAPSULES G-1, G-4 AND G-8 IN F-1 (X094A) EXPERIMENT

Type of Precision Scan	G-1	G-4	G-8
Axial Scans			
Upper fuel-blanket interface	X (0.1)[a]	X (0.05)	X (0.1)
Lower fuel-blanket interface	X (0.05)	X (0.1)	X (0.1)
Diametral Scans			
Upper fuel-blanket interface			
In fuel region	X (0.01)	X (0.01)	---
In blanket region	X (0.01)[b]	X (0.01)	---
Lower fuel-blanket interface			
In fuel region	---	---	---
In blanket region	---	---	X (0.01)

[a] Numbers in parentheses are the scanning intervals in inches.

[b] Two gamma scans were carred out in the blanket region of G-1—the first 1/2 in. above the interface and the second 1 in. above the interface.

Preliminary analysis of the gamma spectrometry data was made at Aerojet Nuclear Company, Idaho Falls, Idaho. Rough scanning of the computer-generated plots has shown no unusual behavior. The following general phenomena have been noted:

1. As in the interim examination at 25,000 MWd/Te, Cs^{137} and I^{131} exhibit activity peaks at the fuel-blanket interfaces; Ba^{140}/La^{140} exhibit peaking at the fuel-blanket interfaces in the high-temperature rod (G-1) but not in the reference temperature rod (G-4).

2. Cesium-137 and iodine-131 have diffused from the fuel into the fuel end of the blanket region. The depth of penetration does not seem to be a significant fraction of the blanket length. Most of the fission product activity in the blanket was generated in situ.

3. As in the earlier interim examination, Cs^{137} and I^{131} have been concentrated at the fuel-cladding interface.

4. There is Cs^{134} in the charcoal traps. Cesium-134 is not a fission product; it is produced by activation of Cs^{133}, which migrates to the traps as Xe^{133}. The presence of Cs^{134} in the trap is therefore expected. No volatile fission products were found in the trap to date, but the Cs^{137} activity may be slightly above background.

5. In the first interim examination at 27,000 MWd/Te burnup, the behavior of Te^{132} was thought to have followed that of iodine. During the second interim examination, the tellurium data are even more scattered than those shown previously, but there is no indication that the behavior of tellurium and iodine is analogous.

Further analysis of these data will be carried out at GGA on the Sigma II computer.

Postirradiation examination of the fuel rod in capsule G-3, which was removed during the first interim examination of the F-1 (X094) experiment at an exposure of 27,000 MWd/Te, is progressing at ANL.

The flux monitors and several of the SiC temperature monitors were removed from the G-3 capsule hardware and readied for shipment to GGA. The fuel-rod plenum was punctured and the volume of gas extracted from the fuel rod was 58.5 cm^3 STP. By backfilling the rod with gas, the fuel-rod void volume was determined to be 22.1 cm^3, which is larger than the computed volume of 19.8 cm^3.

Flow tests through the G-3 fuel rod indicated free flow past the charcoal trap in the plenum region (40 ml/sec at a pressure of 30 in. of water), free flow in the blanket region (8 ml/sec at a pressure of 49 in. of water), and free flow up the central void of the fuel column (42 ml/sec at a pressure of 7 in. of water). However, the flow was restricted at each end of the fuel pellet column. At the interface of the solid blanket pellets and the annular fuel pellets at each end of the fuel column, the flow was only 0.3 ml/sec at a pressure of 50 in. of water. The flow restrictions at the ends of the G-3 fuel column are not as extensive as those seen previously at the ends of the annular fuel column in the GB-9 capsule experiment (0.1 ml/sec at 50 in. of water[3], but they appear to be similar in nature.

Preliminary optical microscopy has been completed on five samples cut from the G-3 fuel rod. The most notable feature revealed was the lack of obvious grain boundary attack of the cladding at the fuel-cladding interface. There was evidence of only minor uniform or matrix attack of the cladding to a depth of approximately 0.0003 in. as shown in Figs. 5.2 and 5.3. No attack of any type was observed in a longitudinal section from the bottom end of the rod, but some minor attack was seen at other elevations where the calculated cladding inside temperatures were above ~700°C. Electron microprobe analyses will also be performed to determine if there are fission products present in the cladding grain boundaries that are not apparent with optical microscopy. Transverse sections through three axial locations along the rod showed columnar grain growth to the extent expected in a rod irradiated at a peak rating of 15.5 kW/ft (see Fig. 5.4).

Examination of the top and bottom longitudinal sections (Figs. 5.5 and 5.6) shows that the central void of the annular fuel pellets was almost closed at the ends of the fuel column. The restriction in the central void

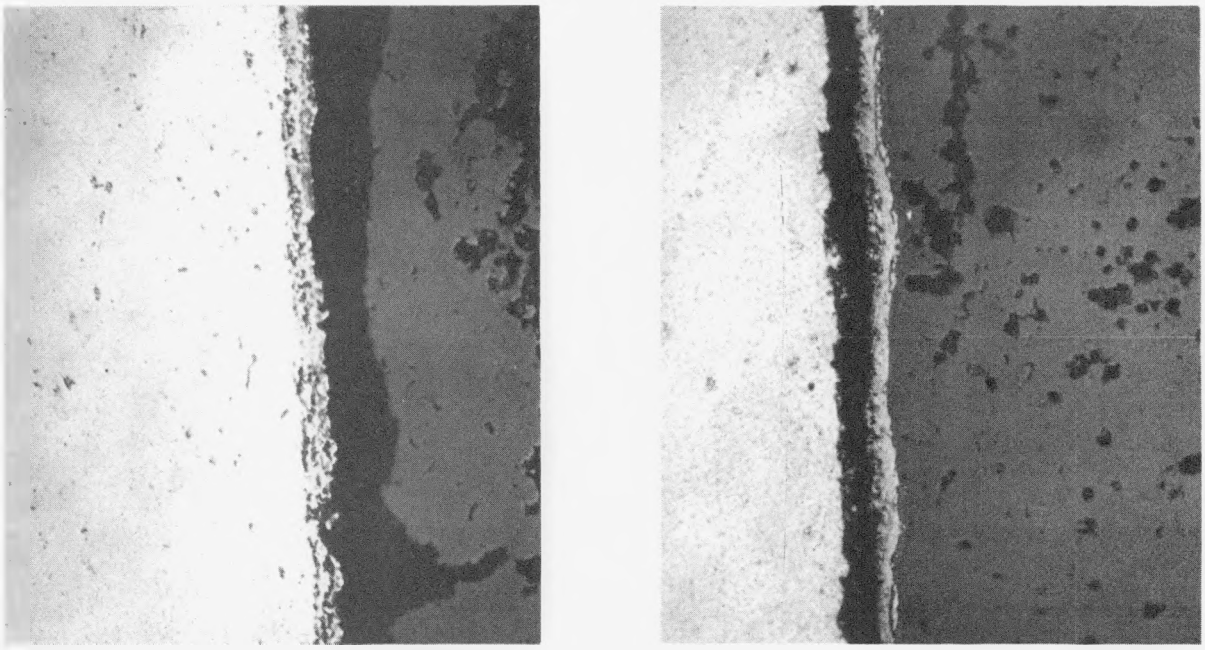

500X 500X

Fig. 5.2 Typical cladding attack in the top transverse section 10-3/4 in. above bottom of fuel column in capsule G-3

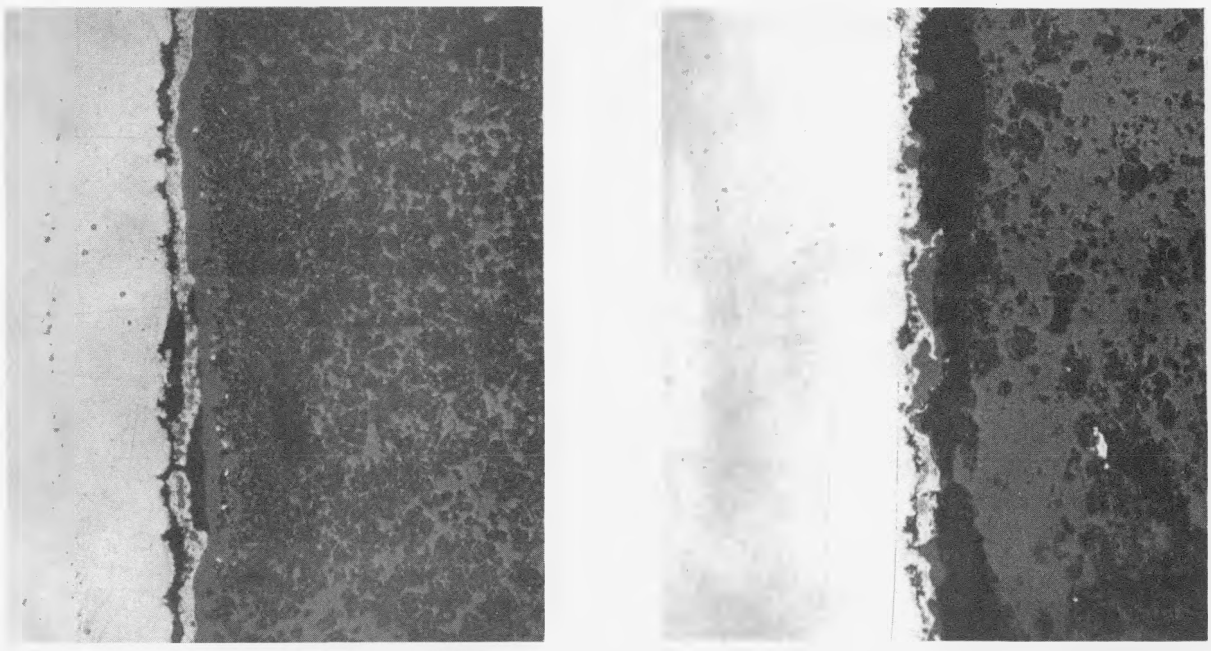

500X 500X

Fig. 5.3 Typical cladding attack in the top longitudinal section of fuel column in capsule G-3

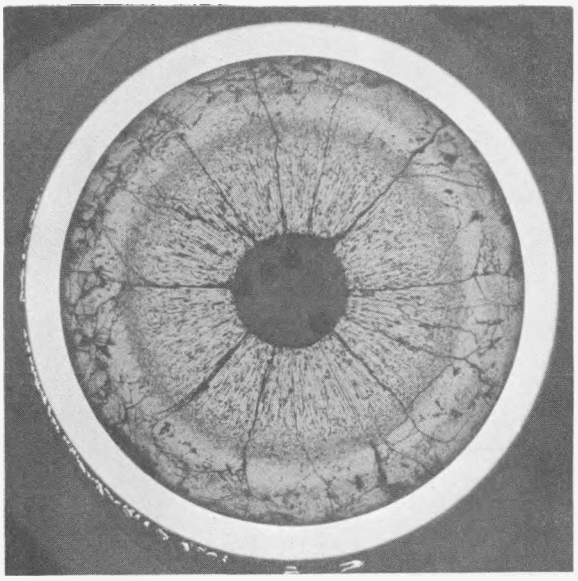

Section taken 10-3/4 in. above bottom of fuel column

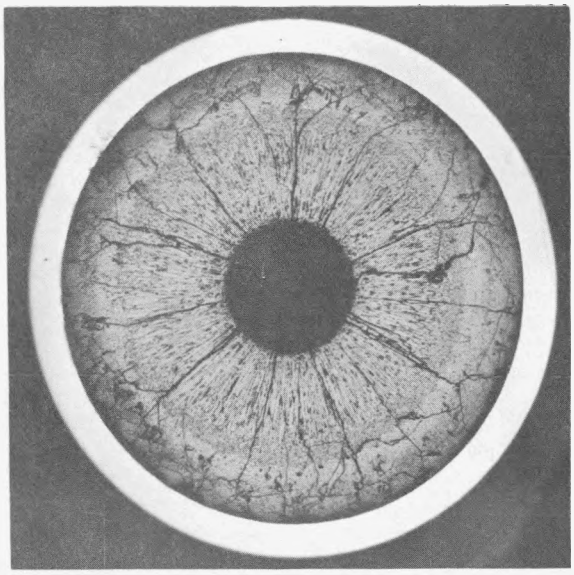

Section taken 6-7/8 in. above bottom of fuel column

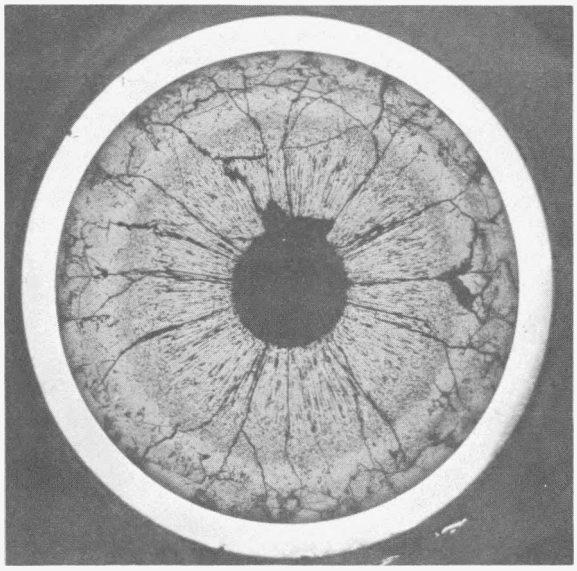

Section taken 3-3/8 in. above bottom of fuel column

Fig. 5.4 Transverse sections of rod in capsule G-3

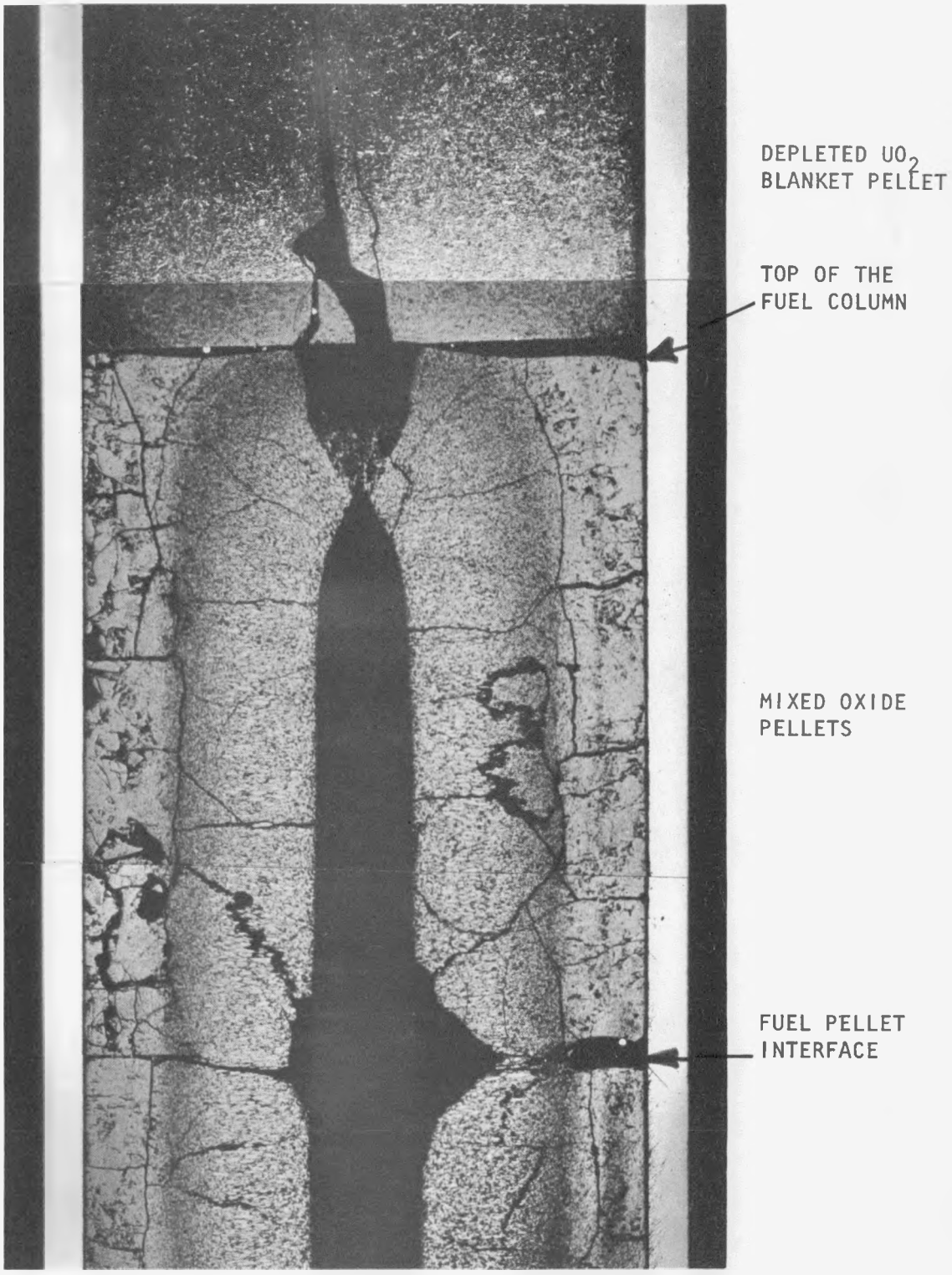

Fig. 5.5 Top longitudinal section of fuel column in capsule G-3 showing vapor-phase transport of mixed-oxide fuel to end of fuel column in annular pellet fuel

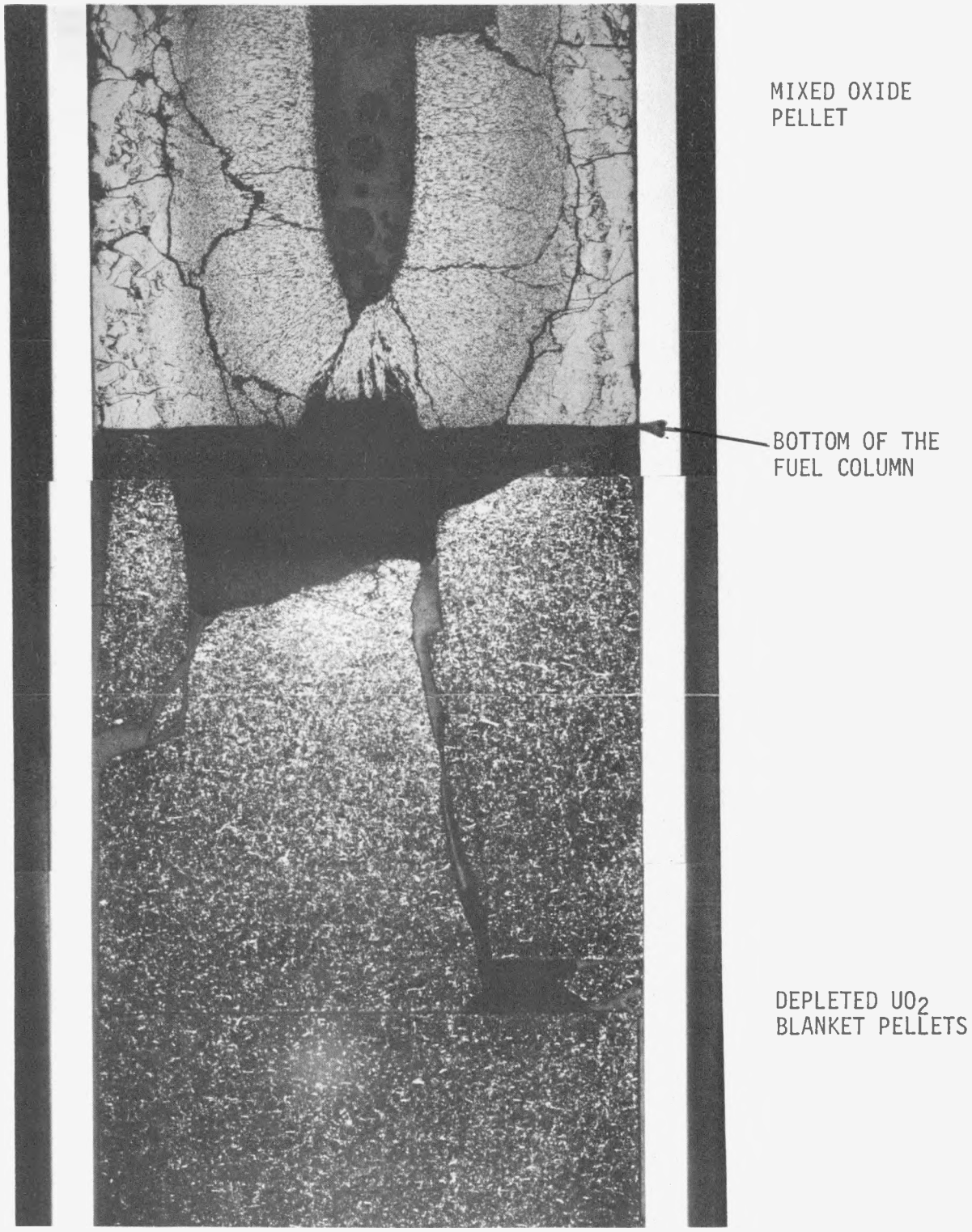

Fig. 5.6 Bottom longitudinal section of fuel column in capsule G-3 showing vapor-phase transport of mixed-oxide fuel to end of fuel column in annular pellet fuel

at the cooler ends of the fuel column appears to result from deposition of fuel material (uranium and plutonium oxides) from vapor species present in the central void during irradiation. This deposition of fuel material in the central void caused the flow restriction that was observed in the flow tests.

5.2.2. Fast-flux Irradiation Experiment F-3

Work continued on the F-3 fast-flux experiment, which has been designed for irradiation in an EBR-II core position (row 4) and which will share a type J19A subassembly with an ANL Group-08 high-temperature chemistry experiment. The initial loading of the subassembly will contain 10 F-3 fuel rod capsules and 9 Group-08 fuel rod capsules. The F-3 fuel rods will achieve neutron exposures up to ~1.5 x 10^{23} nvt at 100,000 MWd/Te burnup. The F-3 fuel-rod cladding temperatures will range from 625°C to 750°C and the linear heat-generation ratings will range from 12 to 15 kW/ft.

The final versions of the F-3 capsule design drawings were sent to ANL and EBR-II. Significant changes made in the design were an increase in the overall capsule length from 40 in. to 40-9/16 in., the addition of a graphite cylindrical sample in the charcoal trap in three fuel rods, and an improvement to the dosimeters to permit easier in-cell disassembly.

During FY 73 chemistry analysis will be limited to verifying the fuel O/M ratio; if it is found to be within tolerance, the fuel will be loaded into fuel rods after they are vacuum degassed.

The assembly of the dosimeters and fuel-rod traps and the roughening of the fuel-rod cladding by chemical etching was completed at GGA. The F-3 fuel-rod hardware (except for some mechanically roughened cladding) has been shipped to ANL for loading and assembly into the fuel rod capsules. The mechanically roughened cladding will be obtained and shipped to ANL in early FY 74.

REFERENCES

1. Findlay, R. R., et al., "The Emmission of Fission Products from Uranium-Plutonium Dioxide during Irradiation to High Burn-up," J. Nucl. Mat., No. 35, 1970 pp. 24-34.

2. Notley, M. J. F., et al., "The Fission Gas Pressures in UO_2 Fuel Elements During Irradiation," Trans. Am. Nucl. Soc., Vol. 8, No. 2, 1965.

3. "Gas-Cooled Fast Breeder Reactor Quarterly Progress Report for the Period August 1, 1972, through October 31, 1972," USAEC, Report GA-A12421, Gulf General Atomic, December 8, 1972.

6. TASK 4700—NUCLEAR ANALYSIS AND REACTOR PHYSICS

Efforts continued on surveillance of LMFBR critical assembly experiments with the objective of establishing an experimentally verified basis for GCFR reactor physics work. Comparison of GGA and ANL calculational methods was begun for selected reactor physics parameters for the sodium-flooded and sodium-voided environment for ZPR-6 Assembly 6-A. Work continued on the definition of goals and requirements of a GCFR critical experiments program. Liaison with ANL continued through the Industrial Participation Program.

6.1. CRITICAL ASSEMBLY ANALYSIS

6.1.1. Analysis of the Sodium-flooded and Sodium-voided Environment of ZPR-6 Assembly 6-A

Twenty-seven-group cross sections have been generated at GGA and ANL. The cross sections for the ANL calculations utilized the SDX code and the Argonne Reactor Computation (ARC) data file system; this system was discussed in the last quarterly report.[1] The GGA cross sections were obtained with the GGC-5 code utilizing the GAROL-GANDY resonance treatments for the resolved and unresolved regions, respectively. The calculational method has been discussed previously.[2] Both the GGA and ANL multigroup cross-section generation methods utilized ENDF/B Version III data.

The comparison of the important cross sections on a group-by-group basis showed excellent agreement for most groups. For example, a comparison of the ANL and GGA multigroup cross sections for Pu^{239} and U^{238} is given in Table 6.1. However, discrepancies have been observed in some groups for several of the other isotopes, in particular iron, especially in the resolved energy region. Most of these discrepancies have been corrected and the others can be traced to differences in the heterogeneity treatment. This work has been curtailed because of funding limitations. However, it

Table 6.1

COMPARISON BETWEEN GGA AND ANL ENDF/B VERSION III MULTIGROUP CROSS SECTIONS FOR U^{238} AND PU^{239}

Group	Lower Energy Bound (ev)	U^{238} $\sigma_{n,\gamma}$		Pu^{239} $\sigma_{fission}$	
		GGA	ANL	GGA	ANL
1	6.06×10^{6} [a]	6.82×10^{-3}	6.94×10^{-3}	2.28	2.67
2	3.68×10^{6}	1.29×10^{-2}	1.27×10^{-2}	1.88	2.15
3	2.23×10^{6}	3.04×10^{-2}	2.98×10^{-2}	2.09	2.30
4	1.35×10^{6}	6.87×10^{-2}	6.73×10^{-2}	2.10	2.25
5	8.21×10^{5}	1.27×10^{-1}	1.25×10^{-1}	1.83	1.94
6	4.98×10^{5}	1.27×10^{-1}	1.26×10^{-1}	1.65	1.68
7	3.34×10^{5} [b]	1.19×10^{-1}	1.18×10^{-1}	1.58	1.60
8	1.83×10^{5}	1.35×10^{-1}	1.35×10^{-1}	1.49	1.50
9	1.11×10^{5}	1.69×10^{-1}	1.69×10^{-1}	1.54	1.53
10	6.74×10^{4}	2.16×10^{-1}	2.16×10^{-1}	1.62	1.62
11	4.09×10^{4}	3.42×10^{-1}	3.34×10^{-1}	1.69	1.68
12	2.48×10^{4}	4.24×10^{-1}	4.30×10^{-1}	1.72	1.70
13	1.50×10^{4}	5.40×10^{-1}	5.25×10^{-1}	1.78	1.75
14	9.12×10^{3}	6.35×10^{-1}	6.28×10^{-1}	1.91	1.88
15	5.53×10^{3}	7.19×10^{-1}	7.32×10^{-1}	2.14	2.11
16	3.35×10^{3}	7.54×10^{-1}	8.26×10^{-1}	2.43	2.41
17	2.03×10^{3}	1.05	9.40×10^{-1}	2.99	2.63
18	1.23×10^{3}	0.949	8.98×10^{-1}	4.32	3.80
19	7.48×10^{2}	1.23	1.14	5.55	5.03
20	4.54×10^{2}	1.22	1.13	7.82	6.77
21	2.75×10^{2}	1.09	1.05	8.29	7.72
22	1.01×10^{2}	1.75	1.36	11.4	11.7
23	3.73×10^{1}	1.73	1.36	22.5	28.7
24	1.37×10^{1}	6.47	4.21	10.2	9.6
25	5.04	2.44	1.91	20.5	22.8
26	0.682 [c]	0.767	1.07	8.43	6.67
27	0.414 [d]	0.429	1.97	14.5	86.7

[a] GGA upper bound is 1.5×10^{7}; ANL upper bound is 1.0×10^{7}.

[b] ANL lower bound is 3.02×10^{5}.

[c] ANL lower bound is 1.86.

[d] ANL lower bound is 0.0.

is expected that this work will continue at the beginning of FY 74. The final comparisons should therefore be available in the next quarterly report.

6.1.2. Comparison of GGA and ANL Perturbation Codes

A series of calculations are under way to compare the GGA perturbation calculational routines. These calculations involve the calculation of helium worth, boron worth, and fissile worths in the 300-MW(e) GCFR. Previous calculations were made with ENDF/B Version II cross sections at GGA and with Version III cross sections at ANL. The calculated helium worths differed by as much as ± 20%. Cross sections have been prepared but final calculations are being delayed until the observed differences between the GGA and ANL multigroup cross sections for ZPR-6 Assembly 6A are resolved.

6.2. ANL LIAISON—GCFR CRITICAL ASSEMBLY PLANNING

The specific needs in the area of physics design verification have been reviewed for the 300-MW(e) GCFR. Key areas have been identified for which specific resolution is desired and in which design considerations presently lack the support of direct experimental verification. A program of critical assembly experimentation has been designed to focus on the unique features of the GCFR concept where extrapolation from past or current LMFBR critical assembly programs cannot provide definitive answers. The program is described in a draft of a report prepared by GGA. This report is currently being reviewed for comments and suggestions by the Fast Reactor Experiments staff at ANL.

The document briefly covers the nuclear design of the 300-MW(e) GCFR and discusses the projected critical assembly program, concentrating in some detail upon the priority tasks. Priority tasks have been defined as those that have significant impact on the safety and licensing procedures for the 300-MW(e) GCFR; these tasks will therefore receive primary attention. Performance-related tasks (those which bear less directly upon safety and licensing aspects but have direct impact upon engineering design and core performance) are assigned the next highest priority. Measurements designed to extract design validations from the criticals program are discussed.

As presently envisioned, the critical experiment program would consist of two assemblies and their variants prior to an engineering mockup critical assembly. The first assembly is expected to be a geometrically clean benchmark assembly in which such effects as steam entry, control-rod worths, and void-channel streaming can be studied without multizonal complications. The second critical assembly would be a modified zoned assembly in which the ability to accurately predict power distributions would be examined.

Special material and equipment needs of the program that would have signficant impact on program costs are also discussed (to the extent that they are now known). Finally, the preliminary schedule and interaction with LMFBR plans for the available facilities has been examined.

REFERENCES

1. "Gas Cooled Fast Breeder Reactor, Quarterly Progress Report for the Period November 1, 1972 through January 31, 1973," USAEC Report GA-A12530, Gulf General Atomic,

2. Pellaud, B., "The Physics Design of the Gas Cooled Fast Breeder Demonstration Plant," USAEC Report GA-10509, Gulf General Atomic, August 29, 1971, Chapter 3.